Spatial Heterodyne Imager for Mesospheric Radicals on STPSat-1

Christoph R. Englert,[1] Michael H. Stevens,[1] David E. Siskind,[1] John M. Harlander,[2] and Frederick L. Roesler[3]

[1] The Spatial Heterodyne Imager for Mesospheric Radicals (SHIMMER) was a high-resolution, near ultraviolet spectrometer that imaged the Earth's limb for 2.5 years between March 2007 and October 2009. The instrument used the Spatial Heterodyne Spectroscopy technique for the first time on a satellite and successfully demonstrated its capabilities. SHIMMER measured the solar resonance fluorescence of the OH $A^2\Sigma^+$-$X^2\Pi$ (0, 0) band around 309 nm, which allows the retrieval of mesospheric OH density profiles. It also measured the Rayleigh scattered background from the clear atmosphere and solar scattering from polar mesospheric cloud particles. We present details on the SHIMMER mission, the payload design, and the data analysis. A comparison between SHIMMER and concurrent Microwave Limb Sounder OH data shows good agreement between 60 and 90 km altitude for several latitudes and seasons. We also find good agreement of the SHIMMER OH densities and standard photochemical model calculations between 60 and 80 km. We find no evidence of a 25%–35% mesospheric OH deficit, previously reported using Middle Atmosphere High-Resolution Spectrograph Investigation (MAHRSI) OH data. However, independent analysis of Rayleigh scattered background signals observed by SHIMMER and MAHRSI under similar lighting conditions revealed that MAHRSI radiances are systematically smaller than SHIMMER radiances by 24%. Although this difference is well outside of the combined uncertainties for both experiments, the agreement of SHIMMER OH with Microwave Limb Sounder OH and standard photochemistry results, together with our Rayleigh scattering comparison, suggests an unidentified MAHRSI calibration problem that effectively eliminates the mesospheric OH deficit reported using MAHRSI observations.

1. Introduction

[2] The hydroxyl (OH) radical plays a critical role in our understanding of mesospheric chemistry. It is important to the catalytic destruction of ozone [*Allen et al.*, 1984] and also serves as a proxy for upper mesospheric water vapor [e.g., *Summers et al.*, 2001]. The mesospheric OH measurement is challenging due to its low concentration (parts per billion) and because OH is very sensitive to variations in local time [*Rodrigo et al.*, 1986] so that comparisons between different experiments must be made with care [e.g., *Englert et al.*, 2000; *Canty et al.*, 2006; *Pickett et al.*, 2006].

[3] Only two profiles of mesospheric OH were reported until the mid-1990s [*Anderson*, 1971; *Morgan et al.*, 1993], when the Middle Atmosphere High-Resolution Spectrograph Investigation (MAHRSI) obtained the first global maps of OH during two space shuttle missions [*Conway et al.*, 1996, 1999, 2000]. These MAHRSI observations indicated that mesospheric OH densities were 25%–35% lower than standard photochemical model predictions and prompted suggested changes to key reaction rates controlling mesospheric OH abundance [e.g., *Summers et al.*, 1997]. However, subsequent to the MAHRSI missions, a variety of independent satellite observations, including data from the Microwave Limb Sounder (MLS) [*Pickett et al.*, 2006, 2008] and from the Optical Spectrograph and Infrared Imaging System (OSIRIS) [*Gattinger et al.*, 2006], have indicated much better agreement with standard photochemistry, thus introducing considerable uncertainty into the state of our knowledge of mesospheric photochemistry.

[4] A resolution of this question was the key scientific objective of the Spatial Heterodyne Imager for Mesospheric Radicals (SHIMMER), the subject of this paper. Indeed, preliminary results from SHIMMER for July 2007 showed excellent agreement between peak OH densities and the standard model at 74 km, although significant local time-dependent differences existed at higher altitudes [*Englert et al.*, 2008]. However, the overall objectives of SHIMMER were broader than simply HO_x chemistry. SHIMMER's primary programmatic objective was to demonstrate that

[1]Naval Research Laboratory, Space Science Division, Washington, District of Columbia, USA.
[2]St. Cloud State University, St. Cloud, Minnesota, USA.
[3]University of Wisconsin-Madison, Madison, Wisconsin, USA.

		Form Approved
	Report Documentation Page	*Form Approved* *OMB No. 0704-0188*

Public reporting burden for the collection of information is estimated to average 1 hour per response, including the time for reviewing instructions, searching existing data sources, gathering and maintaining the data needed, and completing and reviewing the collection of information. Send comments regarding this burden estimate or any other aspect of this collection of information, including suggestions for reducing this burden, to Washington Headquarters Services, Directorate for Information Operations and Reports, 1215 Jefferson Davis Highway, Suite 1204, Arlington VA 22202-4302. Respondents should be aware that notwithstanding any other provision of law, no person shall be subject to a penalty for failing to comply with a collection of information if it does not display a currently valid OMB control number.

1. REPORT DATE **JUN 2010**	2. REPORT TYPE	3. DATES COVERED **00-00-2010 to 00-00-2010**
4. TITLE AND SUBTITLE **Spatial Heterodyne Imager for Mesospheric Radicals on STPSat‑1**		5a. CONTRACT NUMBER
		5b. GRANT NUMBER
		5c. PROGRAM ELEMENT NUMBER
6. AUTHOR(S)		5d. PROJECT NUMBER
		5e. TASK NUMBER
		5f. WORK UNIT NUMBER
7. PERFORMING ORGANIZATION NAME(S) AND ADDRESS(ES) **Naval Research Laboratory,Space Science Division,Washington,DC,20375**		8. PERFORMING ORGANIZATION REPORT NUMBER
9. SPONSORING/MONITORING AGENCY NAME(S) AND ADDRESS(ES)		10. SPONSOR/MONITOR'S ACRONYM(S)
		11. SPONSOR/MONITOR'S REPORT NUMBER(S)
12. DISTRIBUTION/AVAILABILITY STATEMENT **Approved for public release; distribution unlimited**		
13. SUPPLEMENTARY NOTES		
14. ABSTRACT		
15. SUBJECT TERMS		

16. SECURITY CLASSIFICATION OF:			17. LIMITATION OF ABSTRACT	18. NUMBER OF PAGES	19a. NAME OF RESPONSIBLE PERSON
a. REPORT **unclassified**	b. ABSTRACT **unclassified**	c. THIS PAGE **unclassified**	**Same as Report (SAR)**	**20**	

Standard Form 298 (Rev. 8-98)
Prescribed by ANSI Std Z39-18

Spatial Heterodyne Spectroscopy (SHS) is a technique that is suitable and offers advantages for long-duration space flight applications. The SHIMMER data did not only help to reconcile previous OH solar resonance fluorescence observations by MARHSI but, because the satellite which carried SHIMMER, the Space Test Program Satellite-1 (STPSat-1), was launched into a low inclination orbit, afforded considerable local time coverage not provided by many other satellite experiments such as MLS, OSIRIS, or the suite of instruments on the NASA Aeronomy of Ice in the Mesosphere (AIM) satellite [*Russell et al.*, 2009]. This local time coverage has proved useful for studying diurnal variations of hydroxyl [*Englert et al.*, 2008] and mesospheric clouds [*Stevens et al.*, 2009, 2010; *Eckermann et al.*, 2009].

[5] The goal of the present paper is to give a detailed description of all major aspects of the SHIMMER mission, which extended from March 2007 to October 2009. Section 2 provides background information on the instrument heritage and how the scientific motivation evolved from the MAHRSI project in the 1990s. Section 3 presents a mission overview, and sections 4 and 5 present a detailed description of the instrument and of the radiometric calibration of the data, respectively. Readers who are not interested in the technical details of the instrument or the specifics of the radiometric calibration may choose to skip sections 4 and/or 5. Sections 6 and 7 show how we used data of the solar spectrum and terrestrial Rayleigh scattering to validate the spectral response and resolution and to account for on-orbit changes of the calibration. Investigating the Rayleigh scattering is also significant, because it can be used to perform an additional direct and robust comparison with the earlier MAHRSI data. Thus, it provides us with information that is invaluable when we revisit the so-called "HO$_x$ dilemma" [*Conway et al.*, 2000] in section 8. Section 8 presents new SHIMMER OH data and comparisons with MLS OH data for several latitudes and seasons, thus supplementing and supporting the initial analysis of *Englert et al.* [2008].

2. Instrument Heritage

[6] The SHIMMER project has its scientific roots in the MAHRSI experiment. The MAHRSI instrument flew two 2 week missions onboard the Cryogenic Infrared Spectrometers and Telescopes for the Atmosphere-Shuttle Pallet Satellite (CRISTA-SPAS), which was deployed and retrieved by the space shuttle in November 1994 and August 1997 [*Conway et al.*, 1999, 2000]. MAHRSI's high spectral resolution observations in the near ultraviolet (UV) provided the first global scale mesospheric OH altitude profiles. The necessary spectral resolution drove the mass and size of this conventional grating spectrograph so that it required a large space-based platform, which restricted the number of flight opportunities. For the purposes of the scientific results discussed in the present paper, one key result from MAHRSI was that mesospheric OH was observed to be 25%–35% less than standard photochemical models.

[7] Almost simultaneously with the development of MAHRSI in the early 1990s, it was recognized by one of us (FLR) and Robert R. Conway that the emerging optical technique of SHS [*Harlander et al.*, 1992] would be a good match for the challenge of measuring mesospheric OH from space in the near UV. SHS provides the high spectral res-

olution necessary to unambiguously distinguish the OH resonance fluorescence signal from the Rayleigh scattered background together with the necessary sensitivity in a much smaller and lighter package than a conventional grating spectrograph.

[8] The development of a suitable proof-of-concept SHS spectrometer ensued in the following years culminating in a flight on the space shuttle in 2002 [*Cardon et al.*, 2003]. This proof-of-concept instrument was also called SHIMMER. Its SHS interferometer included a beamsplitter, field widening prisms, and gratings all held by a 7 kg Vascomax steel structure to provide mechanical support and adjustments and to ensure the tight mechanical tolerances of the interferometer. The instrument was hard mounted on the orbiter's crew hatch window and was operated via a laptop computer by an astronaut. The pointing was accomplished by adjusting the orbiter's attitude using the measured UV limb profile as a guide. The instrument performed as expected and high-resolution spectra were gathered showing OH fluorescence lines and the highly structured solar background. However, there is evidence that on-orbit contamination of the shuttle window compromised the data and prevented the retrieval of OH altitude profiles from these observations [*Cardon et al.*, 2003].

[9] In order to minimize the size and weight of the interferometer and to further improve its robustness, a monolithic interferometer was designed and built with similar spectral resolution as MAHRSI and appropriate throughput for on-orbit observations of mesospheric OH [*Harlander et al.*, 2003]. LightMachinery, Inc., of Ottawa, Canada, fabricated the interferometer. The optical components of this interferometer were assembled by optically contacting the field-widening prisms, gratings, and appropriate spacers to a hexagonal beamsplitter. While this approach does not allow for any postassembly adjustments, it also means that, except for thermal effects, the interferometer also cannot be misaligned, thus providing a major advantage for space flight instrumentation. Moreover, since the optical contacts do not require any adhesives, the problem of controlling the adhesive layer thickness and parallelism is avoided. This interferometer is the key optical element of the SHIMMER on STPSat-1 spectrometer (henceforth, SHIMMER).

3. SHIMMER Mission

[10] SHIMMER, the primary payload of STPSat-1, is a joint program between the Naval Research Laboratory and the Department of Defense Space Test Program (STP). The STPSat-1 bus was built by AeroAstro, Inc., and it also hosted the Scintillation and Tomography Receiver in Space (CITRIS) payload [*Bernhardt and Siefring*, 2006; *Bernhardt et al.*, 2010; *Siefring et al.*, 2009].

[11] On 7 March 2007, STPSat-1 was launched from Cape Canaveral, Florida, on an Atlas V launch vehicle as part of the STP-1 mission. It was injected into a circular orbit at 560 km altitude and 35.4° inclination. SHIMMER imaged the limb and its line of sight was directed perpendicular to the satellite's velocity vector toward the summer pole so that it observed the Earth's mesosphere up to about 57° latitude. Until the end of the nominal mission in May 2008, the spacecraft was operated from Kirtland Air Force Base, New Mexico. Subsequently, for an additional 1.5 years, it was
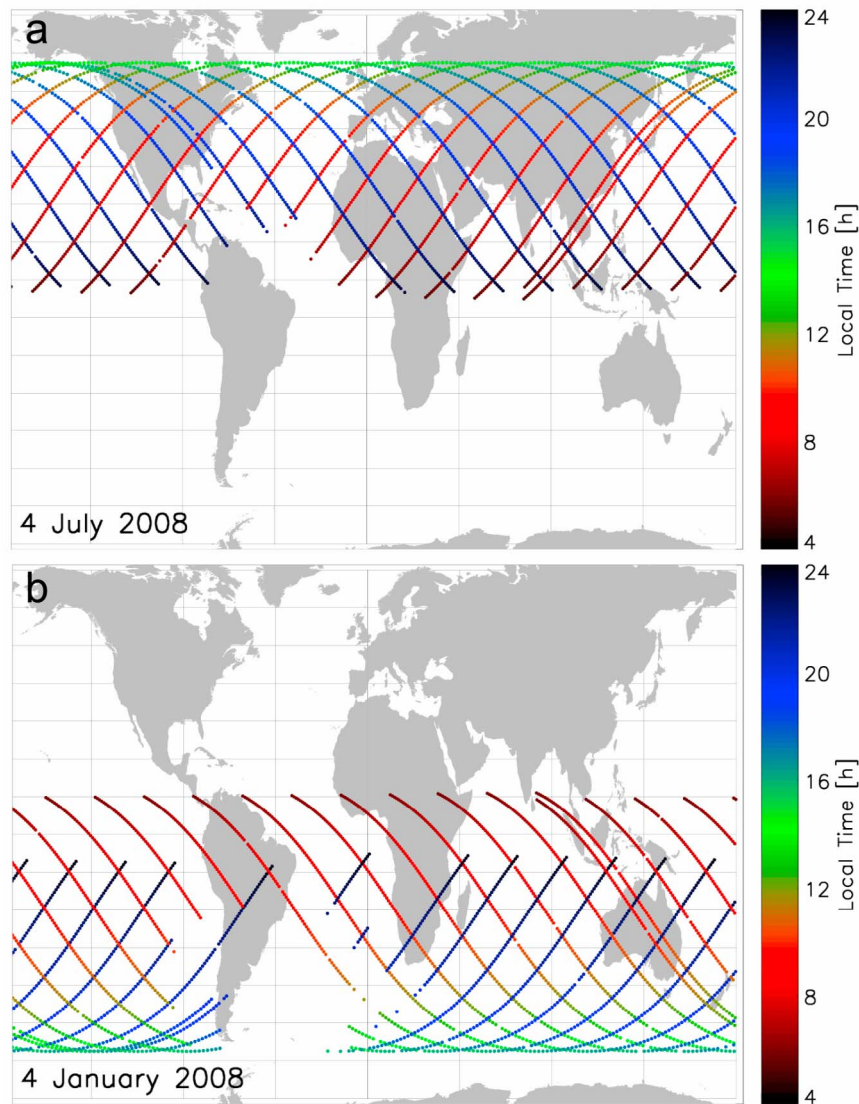
Figure 1. Two examples of the SHIMMER geographic and local time coverage. (a) Every filled circle represents a SHIMMER limb profile that was taken on 4 July 2008, successfully downlinked, and processed. The color of the circle indicates the local time of the measurement. (b) Similar to Figure 1a, but for 4 January 2008. Because of the semiannual yaw maneuver, the SHIMMER coverage is shifted to the north (south) in the boreal (austral) summer. The local time precession of SHIMMER is about 30 min/d. The missing data off the coast of South America are due to the contamination of the SHIMMER detector signal by high-energy particles within the South Atlantic Anomaly.

operated by NRL from the Blossom Point Satellite Control and Tracking Station, Maryland. The STPSat-1 and SHIMMER missions ended on 7 October 2009.

3.1. SHIMMER Measurement Approach

[12] SHIMMER observed the solar resonance fluorescence OH $A^2\Sigma^+$-$X^2\Pi$ (0, 0) band around 309 nm, which is the identical band that was observed by the MAHRSI instrument [*Conway et al.*, 1999]. The only difference is that the SHIMMER passband used for the OH analysis (308.2–309.6 nm) was smaller than that used by MAHRSI (307.8–310.6 nm). The OH emission lines are superimposed on the signal from sunlight that is Rayleigh scattered by atmospheric molecules along the line of sight. Other radiative transfer effects that contribute to the measured signals are the scattering and absorption of the solar flux and the scattering and absorption of the OH emission, both of which increase with decreasing altitude, due to the increasing atmospheric density and increasing ozone density. For a high-resolution spectrum such as from SHIMMER ($\delta\lambda \approx 0.03$ nm), the brightness ratio between the OH fluorescence lines and the Rayleigh scattered background ranges from about unity around 70 km tangent point altitude to only a few percent in the upper stratosphere; depending on numerous factors, like the solar zenith angle, scattering angle, and the OH density. Furthermore, the solar spectrum around 309 nm is highly structured by Fraunhofer lines, so that the *unambiguous* separation of the OH signal from the Rayleigh scattered background signal is facilitated by high spectral resolution.
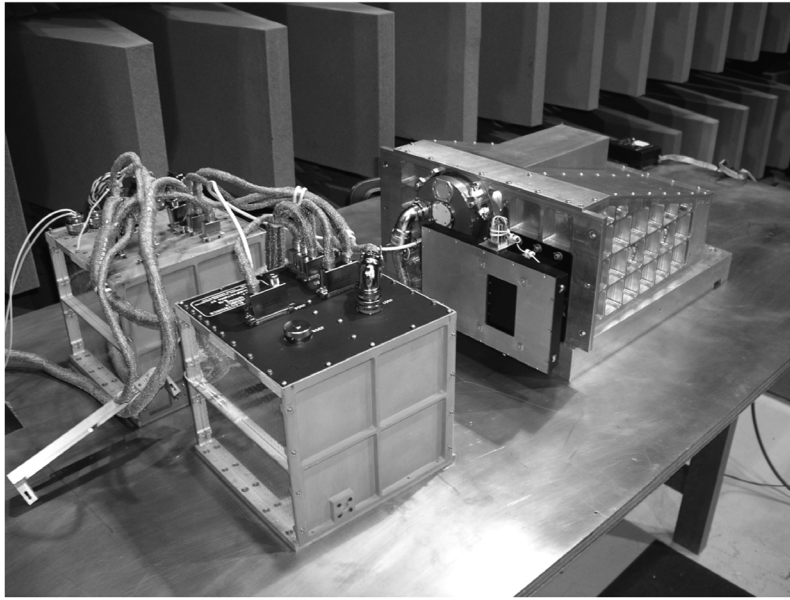
Figure 2. The SHIMMER instrument during electromagnetic interference testing. The cubic assemblies on the left are SECA and SDEA. The assembly on the right contains the optics (SOA). The black rectangle on the front is the entrance aperture of the telescope.

3.2. Observation Geometry

[13] The SHIMMER field of view projected onto the limb was a rectangle subtending about 64 km by 140 km in the vertical and horizontal dimensions, respectively (see section 4.1.3 for more details on the telescope field of view). The vertical dimension was imaged by the instrument, and the signal was binned into 32 elements, which is equivalent to an altitude sampling of about 2 km. The center of the SHIMMER field of view was nominally pointed at a tangent altitude of 65 km but was occasionally adjusted upward to observe the lower thermosphere by changing the satellite attitude.

[14] The center of the SHIMMER field of view was pointed perpendicular to the satellite's velocity direction. Twice a year, the satellite performed a 180° yaw maneuver, so that SHIMMER viewed tangent points to the north or south of the satellite ground track during the boreal or austral summers, respectively. Since the OH resonance fluorescence signal requires sunlight, the SHIMMER observations were limited to the daytime. Figure 1 shows, as an example, the measurement locations for two 24 h periods, one for each yaw configuration.

[15] In the beginning of the mission, the SHIMMER observations were limited to 48 min per orbit, which was the minimum mission requirement. With an image cadence of 20 s, this translates to 124 limb profiles per orbit, where the remaining 20 exposures were generally used to measure the instrument dark field. Depending on the season and the angle between the orbital plane and the vector from the Sun (beta angle), 48 min were not always enough to cover the entire sunlit part of the orbit. Since enough power was available on the satellite, the SHIMMER observation time per orbit was increased to 70 min per orbit for the later part of the mission, which generally allowed measurements from sunrise to sunset at the tangent point regardless of the beta angle (see also section 4.3).

3.3. Local Time of Observations

[16] Since SHIMMER was in a low-inclination, low-altitude orbit, the local time varied steadily with latitude along the orbital track for both the ascending and descending nodes as shown for two example days in Figure 1. In addition, the local time for a particular latitude and node precessed by about 30 min/d for the SHIMMER orbit, so that it took about 24 days for the ascending or descending node to cover 12 h of local time. By contrast, instruments in high-inclination and Sun-synchronous orbits typically dwell on two specific local times that are about 12 h apart and then only rapidly pass through all other local times at the highest latitudes. Furthermore, for higher-inclination orbits at similar altitudes, the orbital precession is smaller, so it takes significantly longer to gather data covering an entire diurnal cycle.

4. Instrument Description

[17] The instrument consists of three major elements: The SHIMMER optics assembly (SOA), the electronics controller assembly (SECA), and the detector electronics assembly (SDEA). The SOA was newly designed and built for SHIMMER, while SECA and SDEA were hardware flown as part of MAHRSI and modified for SHIMMER. Even though SECA and SDEA utilized electronics that were more than a decade old, they presented space-qualified, proven, and existing hardware resulting in significant cost savings. A photograph of the complete instrument is shown in Figure 2. Table 1 summarizes the main SHIMMER mass, size, and power specifications.

4.1. Optics

[18] A design sketch of the optics assembly is shown in Figure 3. Light entered the instrument at the door assembly and passed through the passband filter, telescope, and

SOA mass, size	16.17 kg, 47.0 cm × 40.6 cm × 20.1 cm
SECA mass, size	7.83 kg, 22.9 cm × 21.8 cm × 20.3 cm
SDEA mass, size	6.53 kg, 22.9 cm × 21.8 cm × 20.3 cm
Power	50 W (during observations)

interferometer. The exit optics relayed the signal to the focal plane array (FPA). The total étendue of SHIMMER was approximately 2.7 mm^2 sr, and the overall optical transmission of the instrument, excluding the filter, is 6%–7% depending on the location in the field of view. More details on the optics are given in the following sections.

4.1.1. Door Assembly

[19] The sliding door had three positions: open, closed, and obscured with an acrylic diffuser combined with an aluminized Mylar film, which acted as a neutral density filter. The closed position was used to protect the optics. Moreover, during certain spacecraft anomalies, the door was closed to protect the instrument from accidentally staring at the Sun and potentially damaging the optics or the detector. The diffuser and neutral density filter were used only for taking reference measurements of direct sunlight (see also section 6). These measurements were used to determine the spectral shape of the solar spectrum that was used to separate the OH resonance fluorescence signal from the background (see section 8.1). All atmospheric measurements were performed with the door in the open position. The assembly included a short baffle behind the door, which was comprised of blackened knife edges to minimize scattered light.

4.1.2. Passband Filter

[20] An interference filter was located in front of the telescope aperture to limit the passband to a single sideband of the SHS interferometer. The maximum filter transmittance was 32%, and the half width was 1.9 nm (307.9–309.8 nm). The filter was slightly tilted to mitigate potential fringing between parallel surfaces.

[21] Verification of the SHIMMER field of view in the laboratory revealed that the interference filter possessed nonnegligible optical power, so that an additional compensation lens with a focal length of 17.2 m was introduced at the filter location to compensate for this effect. The SHIMMER passband filter was fabricated by Barr Associates, Inc.

4.1.3. Telescope

[22] The anamorphic telescope consisted of a doublet (T1), a fold mirror (F1), a singlet (T2), another fold mirror (F2), and a triplet lens (T3) as shown in Figure 3. Simple, black anodized baffles were used between the lens assemblies to contain the beam and minimize stray light within the SOA. The telescope imaged the vertical dimension (perpendicular to the limb) onto the gratings in the interferometer. In the horizontal dimension (parallel to the limb), the telescope objective was imaged onto the gratings. This ensured that any horizontal structure within the limb scene, caused, for example, by polar mesospheric clouds (PMCs), did not contaminate the spectral information, which was recovered from the fringe pattern generated by the interferometer in the horizontal dimension. The angular size of the SHIMMER

field of view was determined in the laboratory to be 1.461° × 3.2° (vertical × horizontal), which translated to about 64 km × 140 km on the limb at the STPSat-1 orbital altitude of about 560 km. The vertical angle was measured with high accuracy, since it directly corresponds to the altitude covered by the field of view on the limb. Using the measured angle and orbit altitude, the altitude sampling of SHIMMER is almost exactly 2 km.

[23] The telescope aperture stop was the telescope objective. In the horizontal dimension, the field stop was the singlet telescope lens, while in the vertical the field stop was the image plane. The beam footprints on all the surfaces were rectangular or square. All lenses were antireflection-coated fused silica, and the fold mirrors were coated with a narrow band dielectric reflection coating. The telescope modulation transfer function in the imaging dimension was specified as greater than 70% at 7 cycles/mm.

4.1.4. Interferometer

[24] The SHIMMER interferometer was described in detail by *Harlander et al.* [2003]. Some key aspects of the interferometer design are as follows: All interferometer components were made of Homosil and were optically contacted.
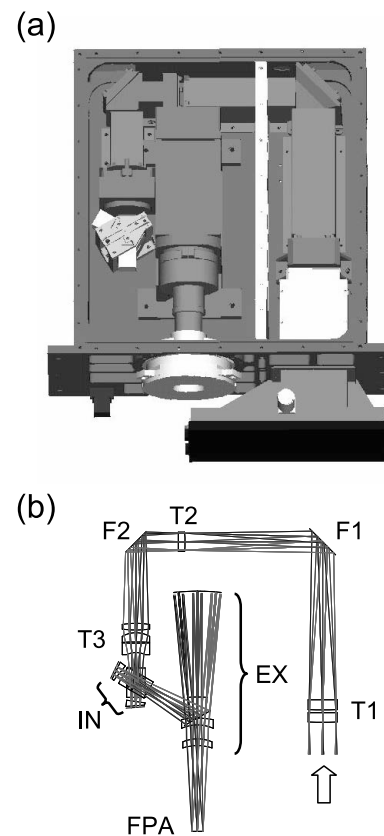

Figure 3. (a) The SHIMMER optics assembly model as viewed from the top without the cover. (b) Raytrace model for the same orientation. T1, T2, and T3 are telescope lenses. F1 and F2 are fold mirrors. IN is the interferometer, EX is the exit optics, and FPA is the focal plane array. Preceding the telescope lenses, T1 (and not shown here) is the interference filter, a lens that corrects for the small optical power in the filter and the door assembly.

The hexagonal beamsplitter shape was chosen to minimize polarization effects (see section 4.1.6). The field-widening prisms had a wedge angle of 13.02°, and the etched, holographic gratings had a groove density of 1200 lines/mm. The illuminated grating surface was about 10 mm × 10 mm, and the vacuum Littrow wavelength as measured on orbit was about 307.48 nm. Details about the effective resolving power that was achieved on orbit are discussed in section 5.

[25] A failure of the interferometer occurred during vibration testing at the instrument level. We document this issue here, since it could not be included in the earlier account by *Harlander et al.* [2003], which was published before the failure occurred. During the vibration test of the SOA, which required a test level of 14.1 g (rms, root mean square), two fasteners of the exit optics assembly completely backed out of their thread, even though the assembly was specified to withstand 18 g rms. More importantly, one grating of the interferometer was found detached after the SOA was opened for inspection. The most likely explanation of the interferometer failure is that one of the free fasteners impacted the grating and the shock detached the grating from the spacer.

[26] The grating suffered some mechanical scratching by this event, but in order to stay within the constrained budget and the project schedule, we decided to have the same grating reattached. (The approach used to correct for these scratches in the analysis of the measured interferograms and their effect on the error budget are discussed in sections 5.1 and 8.1). We find that the contribution to the uncertainty of our OH retrievals due to the grating imperfections is less than 10% near the mesospheric peak of the OH densities (between 70 and 80 km altitude).

[27] We also performed additional vibration testing on a mechanically similar optical contact, where a maximum response of 89.96 g (rms) was recorded in the plane of the contact without compromising the optical contact. This test supports the hypothesis that the grating was detached by the impact of one of the fasteners. To avoid any loose objects from impacting the interferometer again, we installed a shroud around the interferometer. Furthermore, fused silica reinforcement bars were cemented along the interferometer arms for additional mechanical strength. The SOA passed all subsequent vibration testing.

4.1.5. Exit Optics

[28] The exit optics formed an image of the fringes, which are located in the interferometer near the grating planes, onto the charge-coupled device (CCD) detector. We chose to use a conventional Offner assembly, which provided a two-sided telecentric relay with a magnification of unity. Two lenses following the Offner were used to adjust the magnification to 1.33.

[29] The interferometer fringes were aligned perpendicular to the limb (vertically). This drove a stringent requirement on image quality in the horizontal direction and a more relaxed requirement in the vertical dimension, where the image is binned into only 32 slices, corresponding to the 2 km altitude sampling of the limb altitudes. The nominal object size for the Offner assembly is about 10 mm × 10 mm with a 10° square, telecentric beam. The field stop is located at the secondary mirror and is square. The exit optics and telescope lens assemblies were fabricated by Coastal Optical Systems, Inc.

4.1.6. Polarization

[30] The polarization of SHIMMER was measured using the method described by *Kudo et al.* [1970]. This method allows the determination of the polarization of the instrument,

$$P = (T_H - T_V)/(T_H + T_V), \qquad (1)$$

using a combination of measurements with two imperfect polarizers at different orientations. T_H and T_V are the relative response of SHIMMER to the horizontally and vertically polarized signal of a zinc pen ray lamp, which has a bright emission line at $\lambda = 307.59$ nm in the SHIMMER passband. The SHIMMER polarization was determined to be $P = -0.018 \pm 0.005$, which means that the instrument was nearly unpolarized, that is, it was almost equally sensitive to both polarizations. The variation of the instrument polarization across the very narrow passband (≈ 1.9 nm) was assumed to be negligible. By contrast, the MAHRSI polarization was determined to be -75% [*Conway et al.*, 1999], with the maximum response occurring when the E field vector of the signal is vertical (perpendicular to the grating grooves). The main reason for this high polarization of MAHRSI is the more than 4 times higher groove density of the MAHRSI grating compared to the SHIMMER gratings.

4.1.7. Internally Scattered Light

[31] Light from outside the field of view that is scattered inside the instrument is a concern for limb viewing instruments, especially when the dynamic range of the signal brightness is large, both within and just outside the field of regard. As discussed in sections 4.1.1 and 4.1.3, SHIMMER had a short baffle system between the door and the interference filter and simple baffles containing the beam path of the telescope, which helped to minimize scattered light. The beam path between the exit optics and the detector was also baffled, as shown in Figure 3. Compared to a conventional grating spectrograph, an SHS spectrometer offers two additional advantages concerning scattered light. First, only light that is modulated by the interferometer appears in the spectrum after the Fourier transformation of the interferogram, and second, light that is scattered at one grating location is refocused on the detector and does not generally contaminate other altitudes of the limb image.

[32] To assess the scattered light performance of SHIMMER on orbit, we assessed the OH signal in the upper mesosphere around 88 km in the middle of the day during the northern summer, where the OH density is expected to be close to zero. If signal from lower altitudes would be scattered within the instrument and detected at a higher altitude, this altitude region is where it would be most easily detected. The OH profile shown by *Englert et al.* [2008, their Figure 2] shows a negligible OH density at this location, consistent with theory and the OH measurements of the Microwave Limb Sounder (MLS) on NASA's Aura satellite. On the basis of these observations, we conclude that SHIMMER does not suffer from a significant scattered light problem.

4.2. Detector and Electronics

4.2.1. CCD Camera

[33] SHIMMER used a SITe scientific grade SI-003A charge-coupled device (CCD) imaging array, integrated in a

custom camera assembly designed and fabricated by Term Engineering. This CCD had 1024 × 1024 pixels with a pixel pitch of 24 μm. It was thinned, UV antireflection coated, and back illuminated, which resulted in a high enough quantum efficiency (≈48% at 309 nm), so that no additional image intensifier was necessary.

[34] The CCD was mounted within the camera housing together with a low-noise preamplifier board. A thermoelectric cooler (TEC) was used to lower the temperature of the CCD to −40°C or less to minimize the dark current and dark noise. In order to achieve these conditions in the laboratory, the camera housing was thermally isolated from the CCD and could be evacuated to eliminate condensation and convection within the enclosure. The excess heat from the TEC was conducted out of the camera housing by a solid copper heat pipe. Before launch, the evacuation port of the housing was replaced by a light tight, sintered metal disk, which allowed the venting of the housing on orbit.

[35] The integration time of every exposure was controlled by a mechanical shutter that was located in front of the camera housing. The shutter comprised a rotating disk with three open and three closed positions. The accuracy of the exposure time was determined to be 4×10^{-4} s, as verified using an external timer.

4.2.2. CCD Readout Electronics

[36] The SHIMMER CCD was read out by SDEA, which was modified from its MAHRSI configuration [*Conway et al.*, 1999]. Since only about one quarter of the CCD was illuminated by the exit optics, SDEA was configured to read out only the relevant detector area. For nominal operations, an area of 508 × 512 pixels was read, while the second dimension was binned into 32 slices, corresponding to the altitude sampling on the limb. For diagnostic purposes, a mode that allowed reading out the entire CCD was also implemented.

[37] Linearity tests of the CCD, preamplifier, and read out electronics combination revealed a nonnegligible nonlinearity, which was characterized and removed from the data during the raw data analysis. For all types of Fourier transform spectrometers, including SHS, it is especially important to correct for detector nonlinearity, since it can produce ghost features and other artifacts in the recovered spectrum.

[38] In addition to controlling the CCD read out, SDEA also included the controller for the TEC that cooled the CCD. The controller was designed to keep the CCD below a threshold temperature, which could be changed by ground command. During the entire mission, the threshold temperature was kept at −40°C. During times for which the external radiator temperature was low enough so that a CCD temperature below −40°C was achieved without engaging the TEC, the CCD was operated below −40°C, resulting in even lower dark current and noise.

4.2.3. Controller Electronics

[39] SECA included all control electronics for SHIMMER and used an 80C86 microprocessor. It provided all power management, controlled the shutter and door, communicated with SDEA, provided the analog to digital conversion of housekeeping and science data, received, acknowledged, scheduled, and executed commands, and provided science and housekeeping data for transfer to the spacecraft.

4.3. Normal Operations

[40] After the initial on-orbit checkout of SHIMMER in March 2007, the SHIMMER operations were initiated. Throughout the mission, they were only interrupted by occasional spacecraft anomalies, ground station issues, and the semiannual yaw maneuvers.

[41] Every orbit, a sequence of dark, limb, and dark measurements was performed. The image cadence was 20 s, and the integration time was 12 s. Typically, the two blocks of dark measurements were 200 s long, and the limb observations filled the remaining allocated total observation time, which was limited to 48 min in the beginning of the mission and was subsequently increased to 70 min (see also section 3.2). Generally, the first block of dark measurements was started 300 s before sunrise at the 65 km altitude tangent point, and the second block was taken at the end of the OH observations for each orbit. During the PMC seasons, the observations were sometimes shifted relative to sunrise to maximize the coverage of high latitudes.

[42] Preceding several space shuttle launches, the center of the SHIMMER field of view was shifted up from the nominal tangent height of 65 km to about 95 km in an effort to view the shuttle's main engine exhaust plume. Similar observations were previously made serendipitously by MAHRSI and the GUVI (Global Ultraviolet Imager) and SABER (Sounding of the Atmosphere Using Broadband Emission Radiometry) instruments on NASA's TIMED (Thermosphere Ionosphere Mesosphere Energetics and Dynamics) satellite [*Stevens et al.*, 2002, 2005; *Siskind et al.*, 2003; *Meier et al.*, 2010]. However, no strong increases in OH or solar scattering signal that could be unambiguously linked to the shuttle exhaust were identified in the SHIMMER data yet. SHIMMER provided uninterrupted data for time periods after 8 of the 11 shuttle launches that occurred during the SHIMMER mission. For four of these eight launches, SHIMMER pointed toward the south so that the northernmost latitude observed was ~14°N and thousands of kilometers from the injected plume near 33°N. The remaining four launches were between 31 May and 29 August, and all of them occurred after 1600 LT so that the nearest day-lit coincidence with the shuttle ascent profile was between 12 and 20 h after launch and between 0600 and 1400 LT. It is therefore likely that by the time of the SHIMMER overpass, the water was either already transported poleward and away from the northernmost latitudes of observation (~57°N) or enough OH had not yet accumulated in the morning to be observable. A more detailed investigation of weak high-altitude (>80 km) signals that may be linked to a space shuttle exhaust plume is currently ongoing.

5. Data Reduction

[43] The first step in the raw data analysis was to match each time-tagged SHIMMER exposure to the corresponding time-tagged ephemeris information, which locates the measurements in latitude, longitude, and altitude. The ephemeris information is determined from the on-board GPS (Global Positioning System), the star tracker data, and two line element (TLE) sets.

[44] Unless a SHIMMER exposure is severely contaminated by high-energy particle impacts on the CCD, which predominantly occurs within the South Atlantic Anomaly
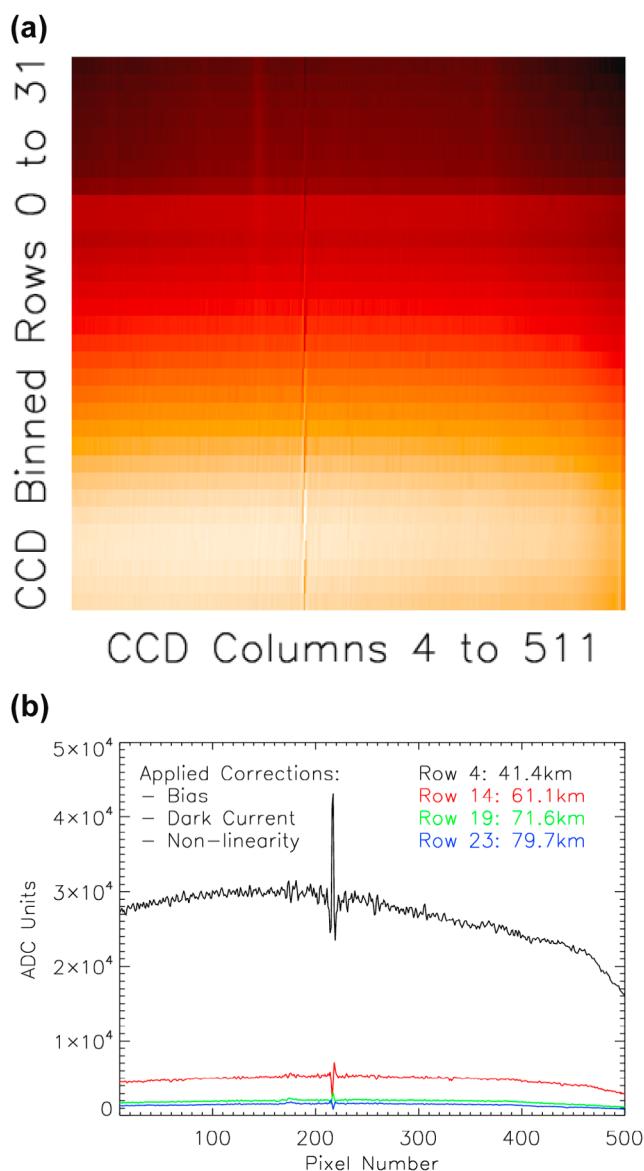
Figure 4. (a) CCD image after corrections for readout bias, dark current, and nonlinearity. (b) Selected rows of the image shown in Figure 4a. The rows are numbered from 0 to 31 from low to high tangent point altitudes on the limb, i.e., row 0 is the bottom row and row 31 is the top row in Figure 4a. Every row covers an altitude interval of about 2 km. For nominal pointing, the centers of row 0 and row 31 correspond to tangent altitudes of ~34 and ~96 km, respectively.

(see also Figure 1), the exposure is routinely calibrated and inserted in the SHIMMER level 1 database. Severely contaminated exposures are identified by a simple threshold criterion, which is applied to the standard deviation of the raw interferogram for two top altitudes in the field of view, where the atmospheric signal is small.

[45] In section 5.1, we describe the calibration algorithm using one particular SHIMMER limb exposure, which was taken on 16 July 2007 at 1047 36 ZUT at a tangent point latitude of 57.16°N, a longitude of 20.76°E (local time, 1204 35), a

solar scattering angle of 98.31°, a solar zenith angle of 35.63°, and the nominal exposure time of 12 s. This particular measurement was chosen because it is part of an averaged spectrum that was previously published [*Englert et al.*, 2008] and it contains the brightest PMC signature measured by SHIMMER on this particular day. Other than the presence of a PMC in this exposure, which only occurs in a small fraction of all SHIMMER observations and does not contaminate the OH retrieval, this is a typical example.

5.1. Interferogram Corrections

[46] The raw CCD data processing starts with the correction for the CCD readout bias, the detector nonlinearity, and the dark current. Information for the bias and dark current corrections is derived from dark measurements taken during the same orbit. At the nominal CCD operating temperature of −40°C and below, the dark current is very small compared to the bias value and the atmospheric signal. The nonlinearity correction is performed using a quadratic function. The parameters of the quadratic function were determined from prelaunch measurements using variable integration times and a constant UV signal level. Figure 4 shows CCD data that are bias, dark current, and nonlinearity corrected.

[47] The next step in the calibration is the flat field correction, which accounts for the response variations between CCD pixels and nonuniformities throughout the entire SHIMMER optics, especially the gratings. The flat field correction is performed according to the "Unbalanced Arm Approach" [*Englert and Harlander*, 2006], using prelaunch laboratory measurements.

[48] Since the gratings are imaged on the focal plane array, any localized grating imperfection, like a scratch, will have a localized effect on the interferogram detected by the CCD. For SHIMMER, the CCD pixel-to-pixel sensitivity variations are small and generally slowly varying with pixel position. However, the effects from grating imperfections are in part large, mostly due to the grating scratches that resulted from the vibration test failure, discussed earlier in section 4.1.4. Thus, it is important to ensure that the grating image is properly registered to the CCD, since a small shift or rotation of the image on the CCD will cause the flat field to change, which means that the laboratory flat field measurements also have to be shifted or rotated to achieve the best possible flat field correction. Therefore, before the flat field correction is applied, the grating image on the CCD is registered to subpixel precision, for each exposure, using grating imperfections as fiducials.

[49] The next step was to identify and correct for high-energy particle effects on the CCD. Even outside of the South Atlantic Anomaly, isolated high-energy particle hits are present in the CCD data, since no special precautions were taken in the camera design to shield the CCD. These sporadic, localized, very high signals are easily identified and are replaced using information from neighboring, unaffected rows.

[50] Subsequently, we performed a phase correction using a simple wavelength-dependent phase shift correction that is familiar from FTS interferograms and which can also be applied to SHS data [*Englert et al.*, 2004]. This method uses a narrow interferogram region around the zero path difference (ZPD) location to determine a low-resolution, wave-
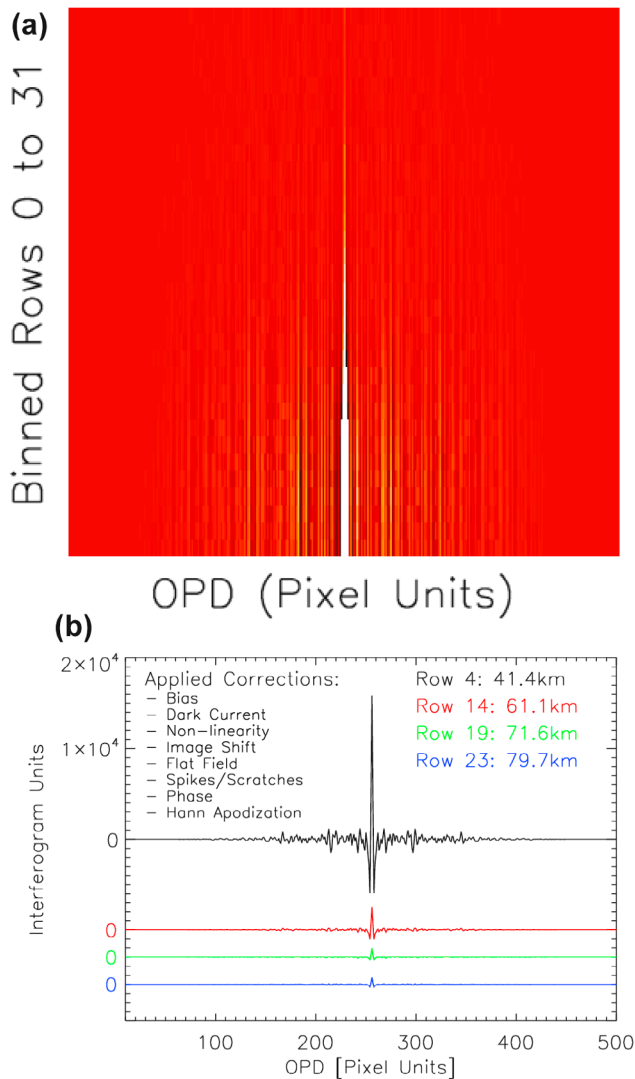
Figure 5. (a) CCD image after applying all corrections listed in Figure 5b. The color scale is chosen to enhance the interferogram features on either side of the zero path location. The large dynamic range of the data results in little color contrast for (top) high row numbers, where the signal decreases, and (left and right) high optical path differences, where the interferogram contrast decreases. (b) Selected rows of the image shown in Figure 5a. The scale of the ordinate is shifted down for rows 14, 19, and 23 as indicated, in order to separate the traces for clarity. Row definitions are the same as in Figure 4.

length-dependent phase shift. To isolate this narrow region around ZPD, we use a Hann function with a total width of 61 interferogram samples. As expected from interferograms that are not sampled symmetrically around the ZPD location, the SHIMMER interferograms show a nearly linear phase shift versus wave number. Once the phase shift is determined, it is easily corrected in the interferogram domain by a convolution with the Fourier transform of the imaginary exponential of the phase shift [*Brault*, 1987].

[51] The final correction of the interferograms is made in regions of severe grating scratches, since these regions might also have degraded modulation efficiencies, which are not properly corrected by the unbalanced arm flat-fielding approach [*Englert and Harlander*, 2006]. These regions are identified in the SHIMMER prelaunch laboratory measurements and are replaced in the flight data, similar to the high-energy particle impact locations on the CCD.

[52] Since the data on one side of the ZPD location (Figure 4a, left) is more severely impacted by the grating imperfections and also shows an unexpected feature that spans over many CCD rows, possibly due to an extended surface contamination of the grating, we have used only the other side of the interferogram for the ensuing radiometric calibration. To keep the format of a double-sided interferogram, the higher-quality side of the corrected interferograms is duplicated on the other side of the ZPD location. Using only one side of the interferogram effectively reduces the throughput of the instrument by a factor of 2 and, assuming shot noise limit, decreases the signal to noise in the interferogram by a factor of square root of 2. Finally, the interferograms are apodized using a Hann function with a total width of 511 interferogram samples. The resulting, corrected interferograms are shown in Figure 5 for the same exposure that is shown in Figure 4.

5.2. Instrumental Line Shape Function

[53] The instrument's line shape function was investigated using a laboratory spectrum of a manganese neon (MnNe) hollow cathode lamp. For this measurement, a holographic diffuser was placed in front of the SHIMMER aperture to improve the homogeneity of the field illumination. The measured interferogram was corrected as discussed in the previous section, and two Ne^+ lines were subsequently isolated in the spectrum with a Hann function and transformed back into the interferogram domain, yielding a virtually monochromatic fringe pattern. The phase of this fringe pattern was determined as discussed by *Englert et al.* [2004], and the interferogram envelope was obtained by dividing the interferogram by the cosine of the phase and subsequent normalization. The Fourier transform of this envelope function is the instrumental line shape function, examples of which are shown for different wavelengths and different detector rows in Figure 6. As expected from self apodization and the Hann apodization of the interferogram, the full width half maximum (FWHM) of the line shape function is slightly wider than two spectral samples. No significant differences were found between the line shapes at the two wavelengths and the different rows. For all following data analysis steps, the line shape was parameterized as a Gaussian function, which is a good representation of the measured line shape (see Figure 6).

[54] In the operational analysis of the on-orbit data, the Gaussian line shape width parameter was determined for each exposure, and it corresponds to a line shape FWHM of about 0.03 nm. The knowledge of the instrumental line shape is of critical importance for the separation of the OH signal from the highly structured Rayleigh scattered solar background, especially at low tangent altitudes, where the background is significantly brighter than the OH features. As discussed below, we find that for the middle and upper mesosphere (60–90 km), the assumption of a Gaussian line shape is adequate. Future work might include a more
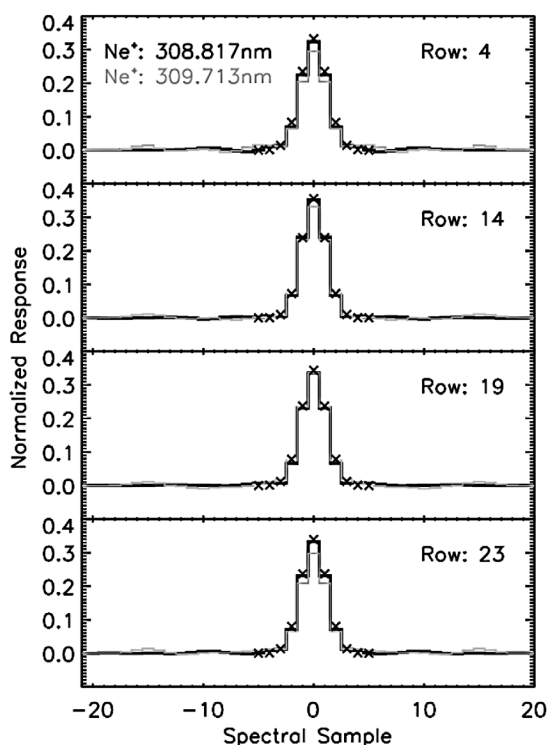
Figure 6. The solid lines are instrumental line shape functions measured in the laboratory using two Ne$^+$ lines at 308.817 and 309.713 nm, which corresponds to about 118 and 189 fringes, respectively, across the detector. The laboratory measurement is analyzed similar to the on-orbit spectra, including the interferogram apodization with a Hann function. The differences in the width of the instrumental line shape functions for different signal wavelengths and detector rows are small. Crosses are the core region of normalized Gaussian functions, illustrating that the line shape function can be approximated and parameterized with a Gaussian function. Row definitions are the same as in Figure 4.

sophisticated treatment of the line shape function to improve the results at lower altitudes.

5.3. Radiometric Calibration

[55] The radiometric calibration of SHIMMER data can be divided into two fundamental parts: The laboratory calibration and the on-orbit corrections that we made to this calibration. All elements of these two parts of the calibration are discussed below, except for the measured on-orbit degradation of the SHIMMER sensitivity, which is discussed in section 7.1.

[56] The laboratory calibration assigns a wave number grid to the retrieved spectrum and provides a radiometric calibration of the spectral intensities based on prelaunch measurements. In order to determine the proper wavelength for each spectral sample, we analyzed the spectrum of a MnNe hollow cathode lamp. In particular, the two Mn lines at 307.963 and 308.133 nm and the two Ne$^+$ lines at 308.816 and 309.713 nm were used to fit the Littrow wave number and the width of the spectral samples. The width of SHS spectral samples is generally equal in wave number units, but not in wavelength units. Even though this difference is small

for a narrow band instrument like SHIMMER, the fit is performed using wave number units. The resulting wave number scale is ultimately converted into wavelength units. The resulting Littrow wavelength (in vacuum) and spectral sample width were 307.318 nm and 1.334 cm^{-1}, respectively. These values are consistent with previously published data for the same interferometer [*Harlander et al.*, 2003]. Small differences are due to thermal effects, and the fact that not the entire grating width is used for the SHIMMER data analysis.

[57] The radiometric calibration is ideally performed using one radiometrically calibrated source that covers the entire passband and fills the entire field of view of the instrument. For SHIMMER, the available calibrated source was the same large aperture integrating sphere that was used for the MAHRSI calibration [*Conway et al.*, 1999]. The sphere was recalibrated by the National Institute of Standards prior to the SHIMMER calibration measurements. The absolute radiance was determined with an accuracy of ±0.4% and with a spectral resolution of 2 nm. The spatial source variation was found to be <1.5% across the area viewed by SHIMMER. However, within the SHIMMER passband, the quartz halogen lamps of the integrating sphere emit two aluminum lines on top of an otherwise slowly varying spectral shape. These lines are not resolved by the NIST measurement, so that for the radiometric calibration of SHIMMER the integrating sphere signal was only used in spectral regions that did not include these emission features. To compensate for this shortcoming, we also made measurements of a deuterium lamp spectrum, which is spectrally flat within the SHIMMER passband but for which only a relative spectral calibration was available.

[58] Figure 7a shows an example of SHIMMER's relative spectral response to the signal of the deuterium lamp, corrected for the small, known variation of the lamp brightness across the passband. By scaling the measured spectra to the correct radiance values, we obtained a single absolute calibration constant. This scaling was achieved by fitting the SHIMMER spectrum to the absolute NIST radiance data of the integrating sphere, in the spectral sample interval between 30 and 50, an area that is not affected by the aluminum lines and that is insensitive to thermal defocus effects (see below). Figure 7b shows such a calibrated spectrum of the integrating sphere. The fact that the calibrated integrating sphere spectrum falls on top of the NIST spectral radiance for spectral samples greater than 50 and away from the aluminum lines verifies the high quality of the relative response curve measured using the deuterium lamp.

[59] To complete the SHIMMER calibration, we applied five on-orbit calibration corrections. They are (1) a shift in Littrow frequency, (2) an adjustment of the spectral sample width, (3) an adjustment of the instrumental line shape function width, (4) a spectral shift in the relative SHIMMER response, and (5) a wavelength-dependent adjustment of the relative spectral response. All these corrections were made simultaneously by fitting the spectra of suitable altitude rows of each exposure to the known spectral shape of the solar spectrum, the shape of the OH solar resonance fluorescence, and an offset term to account for the Ring effect. Sample fit results are presented in Figure 8, where calibrated spectra are shown in black and the sum of the fitted solar background and offset terms are shown in red. Figure 9
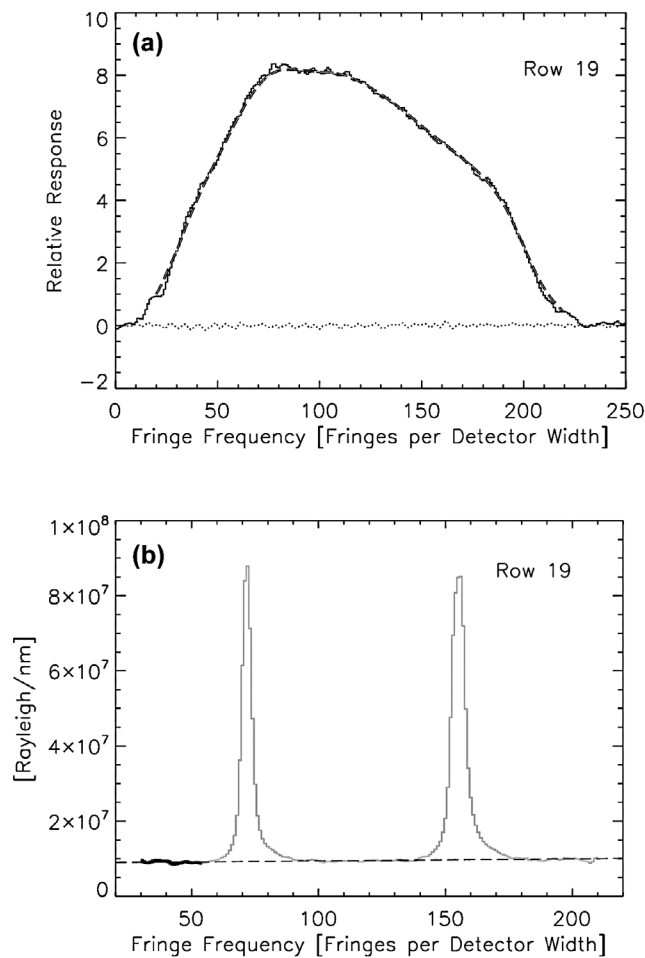
Figure 7. (a) The solid line is the relative spectral response of row 19 versus spectral sample or fringe frequency, measured using a spectrally flat deuterium lamp and corrected for the small variation of brightness across the passband. The dashed line is the measured relative response smoothed with a 20 sample wide boxcar function. The dotted line is the imaginary part of the measured spectrum. The low values of the imaginary part are an indication of proper phase correction. Note that the spectral interval used for the SHIMMER data analysis (308.2–309.6 nm) corresponds roughly to the fringe frequencies between 57 and 167, which means that, within this interval, the response changes by less than a factor of 2. (b) The gray line is the calibrated integrating sphere spectrum. The dashed line is the linear interpolation of the NIST calibration measurement. The interpolated data exclude the areas that are influenced by the aluminum lines. The solid line is the spectral data used to fit the calibration constant, which scales the spectrum to the proper absolute radiance values.

shows the residuals, which are equivalent to the OH resonance fluorescence signals within the measured spectra. Note that the spectra in Figures 8 and 9 are for a single 12 s exposure.

[60] The first correction, the shift in Littrow frequency, is mainly due to thermal effects and the fact that the interferometer is used in vacuum, as opposed to the ambient pres-

sure environment in the laboratory. Thus, small corrections in the effect of the field-widening prisms and the gratings due to the slightly different index of refraction of the surrounding medium, the change in refractive index with temperature, and thermal expansion are expected. For our example exposure, the shift in Littrow wavelength is about +0.16 nm, which is consistent with expectations.

[61] The second correction, the small adjustment in spectral sample width, results from the thermal expansion of the grating and the thermal change in refractive index of the field-widening prisms. For our example exposure, this adjustment is less than 0.2%.

[62] The third correction, an adjustment to the width of the instrumental line shape function, is needed to account for potential on-orbit flat field variations, including a potential difference in the on-orbit illumination of the gratings compared to the laboratory MnNe measurements. A typical value for the on-orbit Gaussian line shape FWHM is 0.03 nm, which is slightly lower (better) than measured in the laboratory, indicating that the on-orbit illumination is more uniform than the illumination achieved by the MnNe lamp in the laboratory.

[63] Fourth, a shift in the relative spectral response is included in the fit to account for the effect of the wavelength change in vacuum and a thermal change in the filter transmittance. For the example exposure in Figures 8 and 9, the optimum response shift is about −0.1 nm.

[64] Finally, we determined the wavelength-dependent adjustment of the spectral response to account for the thermally induced defocus of the exit optics. This effect was observed before launch in the laboratory and can also be
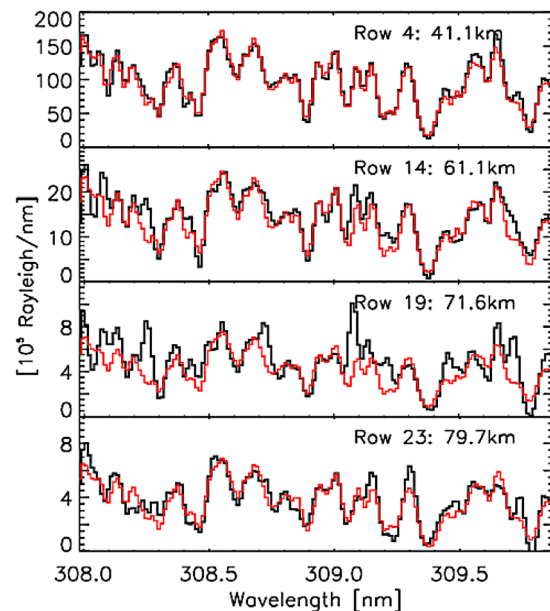

Figure 8. Examples of calibrated spectra from one 12 s exposure and different altitudes (black). The red lines show the solar background and offset contributions of the best fit to the spectra. Note that the dynamic range of the ordinate changes by a factor of 20 from row 4 to row 23. The altitudes corresponding to the row numbers are determined from the pointing data of this particular exposure.
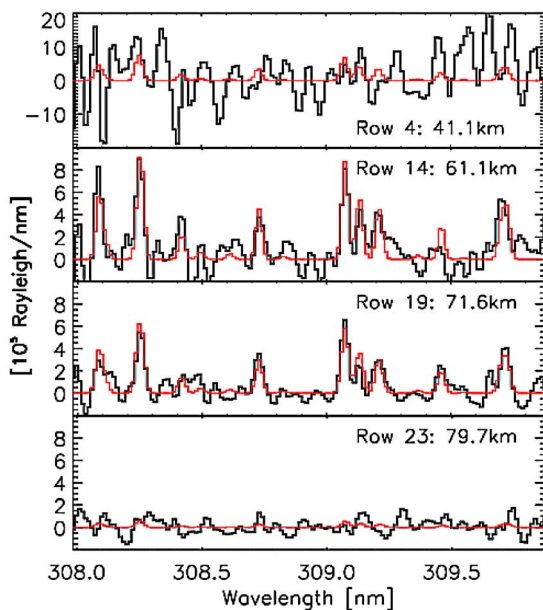
Figure 9. The residuals of the measured spectra and the background and offset terms shown in Figure 8 are given in black. The red lines correspond to the fitted OH resonance fluorescence component. For this single 12 s exposure, the noise dominates at low altitudes (e.g., row 4), where the background signal is high. The OH signal is clearly visible in rows 14 and 19. At higher altitudes (e.g., row 23), OH densities and signals are decreasing and thus the residual spectra are again dominated by noise.

corrected for each exposure using the information within the exposure itself and a parameterization of the change in the spectral response. To parameterize this effect, we consider that it can be modeled by convolving the interferogram with a localized, narrow point spread function that is representative of the angular distribution of the signal that is imaged on the CCD pixels. The Fourier transform of this point spread function results in a function which can be approximated by a low-order Taylor expansion $1 - A \times (x/256)^2$, where the parameter A depends on the point spread function and x is the spectral sample number, starting at $x = 0$ for the Littrow wave number. According to the convolution theorem, the spectrum will be multiplied by this simple quadratic function. As discussed below, by fitting the spectrum for the single parameter A, we can quantify this effect and thus correct for the thermal defocus of the exit optics. For the exposure shown in Figures 8 and 9, A is 0.216, which is equivalent to a response reduction of about 1% at 308 nm ($x \approx 55$) and about 9% at 309.4 nm ($x \approx 165$).

[65] In the operational calibration algorithm, the above on-orbit calibration corrections are performed in three steps.

[66] First, all five correction parameters, the magnitude of the background and OH spectra, and an offset are fitted to the data from tangent point altitudes above about 60 km that contain enough signal to support a meaningful fit. This is typically the altitude range between about 60 and 80 km for a measurement in the middle of the orbital day. CCD rows that correspond to altitudes below 60 km are avoided so that the defocus parameter determination is not contaminated by ozone absorption, which increases for decreasing altitudes and

has a similar, wavelength-dependent effect on the observed spectrum. This step yields a single defocus parameter for each individual exposure. Second, all of the above parameters, except the defocus parameter, are fitted to all rows that contain enough signal to warrant a meaningful fit. This step yields all calibration correction results for these rows. Third, for the remaining rows, e.g., the ones above 80 km that are too dim to warrant a meaningful fit of seven parameters, the calibration uses the defocus parameter of this particular exposure and typical values for the other four on-orbit calibration parameters.

[67] After completing the calibration procedure described above, the calibration results, including the calibrated spectra, are inserted into the SHIMMER database. The fitted spectra shown in Figures 8 and 9 for individual frames are discarded. After the correction for the on-orbit degradation of SHIMMER described in section 7, the calibrated spectra are coaveraged in time and latitude and the resultant-averaged spectra are used to retrieve the OH radiances and density profiles presented here (see section 8).

6. Solar Spectral Shape Measurements

[68] Since the isolation of the OH resonance fluorescence signal from the limb radiance requires the removal of the Rayleigh scattered, highly structured solar spectrum, it is important to verify the shape of the pure solar spectrum as viewed by the SHIMMER instrument. A similar measurement was made with the MAHRSI instrument, which viewed the solar signal reflected by the moon [*Stevens and Conway*, 1999]. Viewing the moon has the advantage that the signal brightness is much closer to the limb brightness than viewing the Sun directly, while the spectral shape of the signal within this narrow spectral band is not changed in any significant way by the reflection on the lunar surface.

[69] Since the orientation of the STPSat-1 startracker did not allow SHIMMER to be pointed at the full moon, SHIMMER was designed so it could be pointed directly at the Sun. For this Sun measurement, an aluminized Mylar, neutral density filter film and a 60° acrylic, embossed light shaping diffuser were placed in front of the telescope. On 21 September 2007, a special maneuver was successfully performed, which allowed SHIMMER to collect 38 exposures of direct sunlight with an integration time of 3.3 s each. The retrieved spectra are presented in Figure 10 for selected rows of the focal plane array. Also shown in Figure 10 is a high-resolution ground-based solar spectrum from the National Solar Observatory [*Kurucz et al.*, 1984], adjusted for the atmospheric effects [*Stevens and Conway*, 1999] and convolved with a Gaussian instrumental line shape function to fit the SHIMMER data. Figure 10 illustrates that no significant differences between the measured spectral shape and the spectral shape expected from the NSO data were found. We use the solar background measurements for each individual row to properly quantify and subtract the Rayleigh scattered signal for each individual altitude (row) of the limb observations.

7. Observations of Rayleigh Scattering

[70] Here we describe the SHIMMER measurements of the total Rayleigh scattered brightness. This simple and direct measurement serves two purposes, which we describe
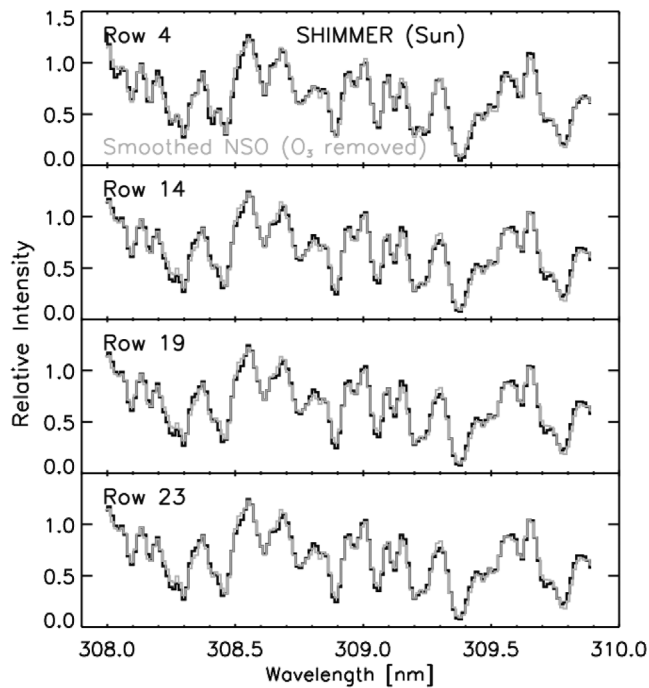
Figure 10. Spectra of an average of 38, 3.3 s exposures of direct sunlight for selected rows are given in black. The gray traces indicate best fit, top of the atmosphere solar spectra that are determined from a ground based measurement and that are convolved with a Gaussian instrumental line shape function [*Kurucz et al.*, 1984; *Stevens and Conway*, 1999].

below. First, it can be used to assess the on-orbit degradation of SHIMMER over the 2.5 year mission length. Second, it provides a valuable transfer standard with which to compare the SHIMMER measurements with MAHRSI data.

7.1. On-Orbit Instrument Degradation

[71] The total Rayleigh scattered brightness versus altitude is a simple and direct data product from SHIMMER, and it can be used to assess the on-orbit degradation of SHIMMER for all observations of the Earth's limb between March 2007 and October 2009. The brightness profile exhibits a peak between 40 and 45 km altitude, which is primarily caused by the increase in Rayleigh scattering and the increase in ozone absorption with decreasing tangent point height. We use the signal of this brightness peak integrated over the spectral region between 308.2 and 308.5 nm.

[72] In Figure 11a, we assemble the peak brightness of limb profiles in a time series covering the entire SHIMMER mission. All of the observations shown in Figure 11a are collected between 15°S and 15°N, because these latitudes are continuously sampled regardless of whether the SHIMMER line of sight is yawed to the north or south, thereby maximizing the temporal coverage. The data are shown as a relative brightness here because we are only interested in the relative degradation from the beginning of the mission, and the daily average is shown in red. A general and expected downward trend is evident, indicating gradual on-orbit degradation. This degradation is most likely caused by the deposition of gas phase contaminants onto optical surfaces, which results in decreased optical efficiency in the UV.

[73] Superimposed on the downward trend in measured brightness shown in Figure 11a is a significant variability on time scales of tens of days, primarily due to the precession of the STPSat-1 orbit and the concomitant change in the scattering angle for the observations, which directly affects the measured Rayleigh scattered brightness. We also find that the annually averaged altitudes corresponding to the peak brightness shown in Figure 11a are all within 0.5 km between 2007 and 2009 (not shown), underscoring the stability of the pointing accuracy throughout the mission.

[74] Figure 11b shows the variation of the relative peak brightness with solar scattering angle using the observations from 2007. The average of all the points is shown, as is the best fit Rayleigh phase function, which dominates the scattering angle dependence of the peak brightness. We use the theoretical Rayleigh scattering phase function to normalize the data in Figure 11a to a 90° solar scattering angle, and this result is shown in Figure 11c. This step significantly reduces the small-scale variability shown in Figure 11a, confirming that it is predominantly caused by the changing observation geometry, i.e., the changing scattering angle. We subsequently find a least squares best fit to the daily average with the functional form $I = I_0 \times \exp(-t/C)$, where I_0 is the intensity at the beginning of the mission and t is the time from launch in days. We find that the best fit to the data yields a value of C that is 1518 (days) as indicated in the frame. To account for the on-orbit degradation, the resultant exponential curve, which is overplotted in Figure 11c, is used to correct all of the SHIMMER data, resulting in an upward correction of about 10% for the data from the summer of 2007 [*Englert et al.*, 2008] and an upward correction of roughly a factor of 2 for the data at the end of the mission. As we will show in section 8.1, a linear scaling of the radiances will result in an approximately similar linear scaling of the OH densities above about 77 km, since the nonlinear effects in the density retrieval are small. The effects at lower altitudes are increasingly nonlinear.

[75] Since we were able to use a very large number of measurements (377,290) to quantify the on-orbit degradation, the resulting uncertainty is small. We estimate the uncertainty of the on-orbit degradation correction to be less than 1%. We use this adjusted data set (SHIMMER Data Version 2) for the remainder of the analyses presented in this work.

7.2. SHIMMER/MAHRSI Comparison

[76] The Rayleigh scattered background brightness can also be used to intercompare the measured background brightness and altitude registration of SHIMMER and MAHRSI, which were observed in the same spectral region. A comparison of their measured Rayleigh scattered background signal can yield insight to any systematic differences between the two measurements, even though they were separated by over a decade in time. The observed background signal primarily depends on the solar scattering angle, the atmospheric density profile, the solar irradiance, and the ozone abundance, which is not a significant factor in the upper mesosphere but increases in importance in the lower thermosphere and upper stratosphere. *Lean et al.* [1997] showed that variations of the solar irradiance over the solar activity cycle near 308 nm are less than 1%. By selecting the similar lighting conditions, time of year, and
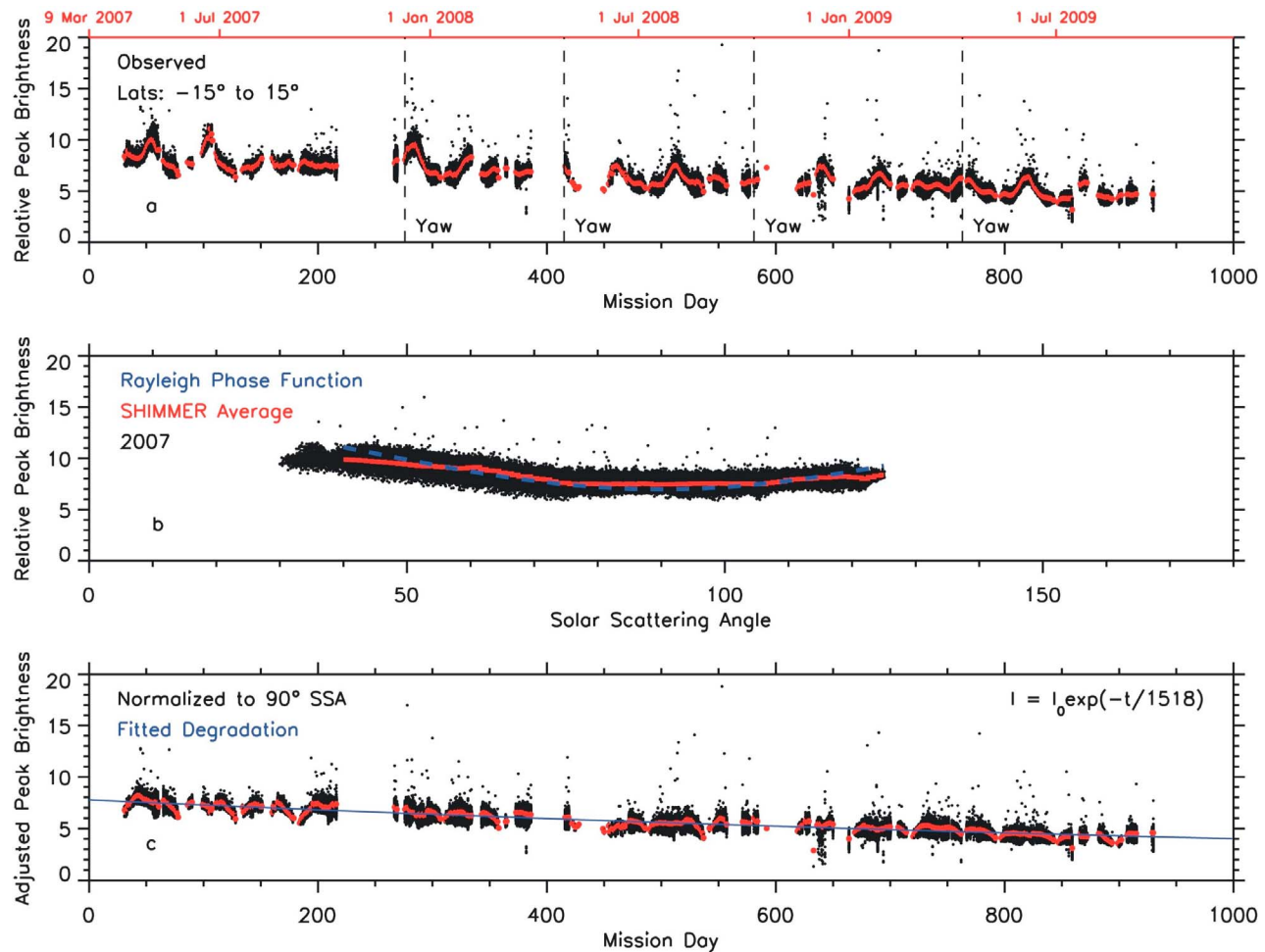
Figure 11. (a) The relative peak brightness of the observed Rayleigh scattered background signal during the SHIMMER mission. Daily averages are shown in red, and a gradual decrease is evident, which we attribute to on-orbit degradation of the instrument. SHIMMER began the mission looking north and perpendicular to the velocity vector of STPSat-1. The days on which SHIMMER reoriented itself to look south (or north) are indicated by the dashed lines. (b) The SHIMMER peak brightnesses of 2007 assembled as a function of solar scattering angle (SSA). The average is shown in red, and the best fit Rayleigh scattering phase function is shown as a blue dashed line. (c) The SHIMMER peak brightnesses normalized to a 90° SSA. Overplotted in blue is a least squares best fit to the daily averages using the functional form indicated in the top right of the frame where t is days after launch.

latitudes for the SHIMMER and MAHRSI measurements, we can ensure similar scattering angles and atmospheric conditions. We use the same spectral interval between 308.2 and 308.5 nm for the analysis of both data sets, and we take the total observed emission within this interval to represent the Rayleigh scattered background. On the basis of the MAHRSI results, the OH signal contribution within this spectral interval constitutes less than 2% of the emission at the peak of the Rayleigh scattered profile in the upper stratosphere and is therefore insignificant for this comparison. Furthermore, the OH signal contribution is expected to be similar for both MAHRSI and SHIMMER measurements. Thus, the following analysis is insensitive to the exact choice of the spectral interval.

[77] In order to ensure the most reliable comparison, we found the lighting conditions in the SHIMMER data set that best matched the MAHRSI observations during its second

mission in August 1997. One complication in this comparison is the polarization of the emergent Rayleigh scattered light. As discussed in section 4.1.6, while SHIMMER was essentially equally sensitive to all polarizations, MAHRSI's sensitivity was a strong function of polarization. Thus, a correction was made to the MAHRSI Rayleigh scattered brightness profiles based on laboratory measurements of the instrument polarization [*Conway et al.*, 1999] as well as the viewing and lighting conditions of the MAHRSI limb scans used [*Conway et al.*, 2000]. The amount of this correction is dependent on the lighting and viewing conditions and is illustrated in Figure 12a. Figure 12a shows the peak Rayleigh scattered brightness for the 34 MAHRSI profiles used in the analysis, both with and without the polarization correction. After correcting for polarization sensitivity, the MAHRSI peak brightnesses have a solar scattering angle dependence that is very close to the Rayleigh phase func-
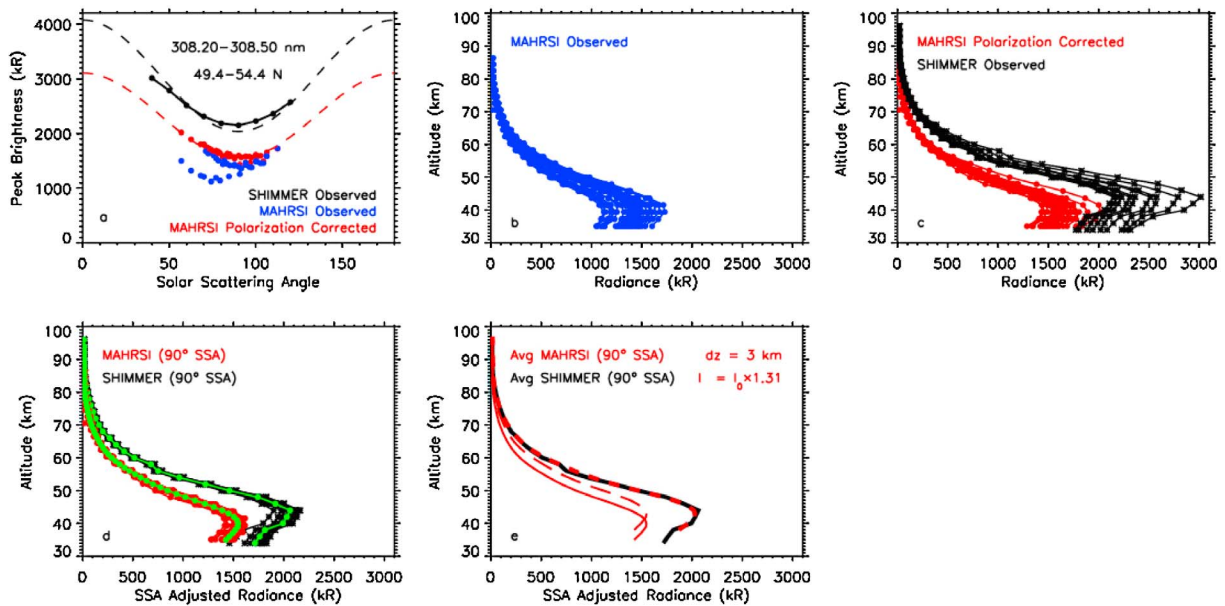
Figure 12. (a) The observed peak brightness of the Rayleigh scattered background observed by MAHRSI between 10 and 15 August 1997 over the indicated spectral range and latitudes (blue symbols). The peak brightnesses corrected for the MAHRSI polarization are also shown (red symbols) as well as the best fit Rayleigh scattering phase function over the observed scattering angles (red dashed line). Also shown are averaged SHIMMER peak brightnesses over the same spectral range and latitudes (black symbols). Each symbol represents an average of 200–1000 limb images between 25 June and 15 July 2007, and the best fit Rayleigh phase function is overplotted (blue dashed line). (b) Brightness profiles observed by MAHRSI corresponding to the blue symbols in Figure 12a. (c) Brightness profiles observed by MAHRSI and corrected for the MAHRSI polarization (red) and the observed SHIMMER brightness profiles corresponding to the black symbols in Figure 12a. (d) MAHRSI (red, polarization corrected) and SHIMMER (black) brightness profiles normalized to a 90° solar scattering angle (SSA). The average of each data set is overplotted in green. (e) Average brightness profiles for MARHSI (red line) and SHIMMER (black line). The results using a 3 km upward adjustment (red, long dash) and a 31% upward correction to the MARHSI average (red, short dash) are also shown. The 31% upward correction corresponds to a 24% underestimate of the background signal by MAHRSI compared with SHIMMER ($1/1.31 \approx 1 - 0.24$).

tion, providing evidence that the polarization correction is reliable. Also shown in Figure 12a is the peak Rayleigh scattered brightness for the SHIMMER profiles over the same spectral region, which are collected over a 3 week period during the 2007 summer. The SHIMMER profiles are averaged between the indicated latitudes in 10° increments of scattering angle, and there are over 200 profiles included in each SHIMMER point shown. Like MAHRSI, the SHIMMER peak brightnesses are largely consistent with the expected Rayleigh phase function. One can see, however, that SHIMMER measurements are systematically higher than MAHRSI profiles despite the fact that both data sets are assembled for the same spectral region, latitudes, scattering angles, and time of year. Since the higher brightness of SHIMMER shown in Figure 12a would convey almost directly to the retrieved mesospheric OH, this has important implications for the reported OH deficit of similar magnitude obtained using the MAHRSI observations. We explore this discrepancy of the Rayleigh scattered signal in more detail below.

[78] Figure 12b shows all the observed MARHSI profiles of Rayleigh scattered light uncorrected for the effects of polarization. The peak brightnesses of these profiles vary between about 1100 and 1700 kR, consistent with the MAHRSI observed peak brighnesses plotted in Figure 12a. Figure 12c shows a comparison between the MAHRSI profiles that are corrected for polarization and the SHIMMER profiles corresponding to the peak brightnesses in Figure 12a. Here one cannot only see the systematic differences between the two data sets but also an altitude offset of about 3 km with the SHIMMER profiles peaking higher than the MAHRSI profiles.

[79] Figure 12d shows the same profiles as Figure 12c, except that they have all been normalized to a solar scattering angle of 90° using the Rayleigh scattering phase functions indicated by the dashed lines in Figure 12a. As expected, this substantially reduces the scatter of both data sets and the average of each of these sets of profiles is overplotted. Figure 12e shows the MAHRSI and SHIMMER average profiles and also the result of raising the MAHRSI profile by 3 km and systematically increasing the MAHRSI profile by 31%. This value of 31% is determined by the fit of the Rayleigh phase functions to the data shown Figure 12a and effectively matches the MAHRSI peak background brightness to the one observed by SHIMMER. Increasing the MAHRSI profile by 31% is equivalent to a 24% background
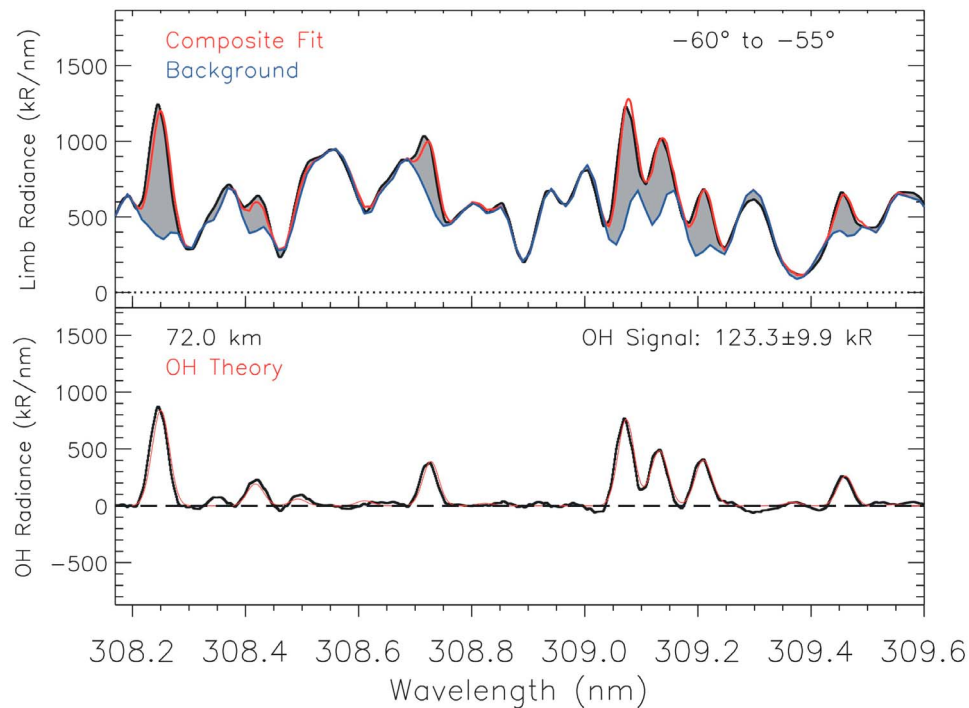
Figure 13. (top) Observed zonally averaged limb spectrum from 6 January 2008 between 55°S and 60°S and at a 72 km tangent altitude (in black). The estimated Rayleigh scattered background is oveplotted in blue, and the composite fit with OH solar resonance fluorescence is overplotted in red. The shaded region shows the OH signal. (bottom) OH solar resonance fluorescence signal in black with the theoretical spectrum overplotted in red. The total intensity over the passband shown is indicated in the top right with the total (systematic and statistical) uncertainty indicated.

brightness underestimate by MAHRSI as compared to SHIMMER (1.31 × [1 − 0.24] ≈ 1). These altitude and brightness adjustments allow agreement between the two data sets to within 10% throughout almost the entire mesosphere. The fact that a simple scale factor and an upward correction of the peak altitude for the MAHRSI observations yield good agreement between the measured Rayleigh background signals from the upper stratosphere to the upper mesosphere suggests that a change in the ozone profile is not the cause for the differences in the SHIMMER and MAHRSI observations, since ozone opacity is not important to the measured signal above 60 km altitude [*Conway et al.*, 1999].

[80] We emphasize that the reported pointing knowledge (±0.25 km) and absolute radiometric calibration (+1.8%, −7.2%) of MAHRSI [*Conway et al.*, 1999] are considerably less than the adjustments that reconcile the Rayleigh scattered brightnesses with SHIMMER. These adjustments are, however, also in excess of the SHIMMER pointing knowledge (1 km) and absolute calibration (altitude dependent; see Figures 15 and 16 in section 8) [*Englert et al.*, 2008].

[81] At this time, we have no further information or evidence on why the MAHRSI and SHIMMER pointing and/or calibration disagree, but it is noteworthy that the magnitude of the calibration correction to MAHRSI would effectively eliminate the OH model excess reported in several previous studies using MAHRSI observations [e.g., *Summers et al.*, 1997; *Conway et al.*, 1999, 2000; *Summers et al.*, 2001]. We furthermore note that a 3 km upward correction to the specific set of 1997 MAHRSI data that were used by *Conway*

et al. [2000, their Plate 2] would improve agreement between the OH observations and model results. This particular report uses the same MAHRSI scans that were used in the comparisons shown throughout Figure 12. These M1AHRSI scans resulted from unique operations that directed the instrument's line of sight to midlatitudes. Thus, they are not necessarily representative for the nominal pointing accuracy of MAHRSI, e.g., due to the potential for variations in the thermoelastic distortions of the satellite and/or MAHRSI for different satellite illumination conditions during these operations. We will revisit these MAHRSI and SHIMMER differences in section 8 when we compare SHIMMER OH observations against both concurrent MLS OH observations and standard photochemical model results.

8. OH Measurements

8.1. OH Radiances and Retrieval of Density Profiles

[82] Our approach to retrieving OH solar resonance fluorescence profiles from the observed limb radiance at each tangent altitude is similar to the approach used by *Englert et al.* [2008] and discussed in detail by *Conway et al.* [1999]. As discussed by *Englert et al.*, the Rayleigh scattered background shape was obtained using special on-orbit operations that allowed SHIMMER to look directly at the Sun through a diffuser and neutral density filter (see also section 5).

[83] An example of the OH radiance retrieval is illustrated in Figure 13, which shows data from 6 January 2008 aver-
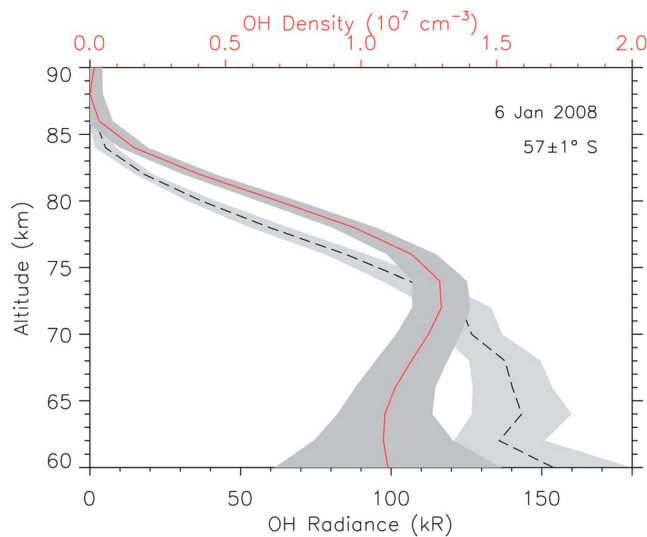
Figure 14. The OH radiance profile (black dashed line) and inverted density profile (red, referenced to the top axis) corresponding to the retrieval at 72 km tangent height shown in Figure 13.

aged between 56°S and 58°S at the fringe of the summer polar region. In Figure 13 (top), the observed signal at a tangent altitude of 72 km is fit with four different components: (1) the spectral shape of the Rayleigh scattered background, (2) the theoretical OH solar resonance fluorescence spectrum convolved with the SHIMMER instrumental line shape function, (3) a small amount of OH prompt emission [*Stevens et al.*, 2008], and (4) a small constant. In Figure 13 (bottom), we have subtracted away the fitted Rayleigh scattered background, the OH prompt spectrum, and the constant to reveal the OH solar resonance fluorescence radiance, which is in excellent agreement with the overplotted theoretical spectral shape of OH. The total OH radiance over the passband is also indicated in Figure 13 (bottom).

[84] We retrieve the OH signal from each tangent altitude in this way, and the intensities are inverted to local OH number densities using the same retrieval algorithm used by *Englert et al.* [2008]. We emphasize here that the OH emission rate factors (g factors) used in the retrieval are identical to those used for the MAHRSI retrievals [*Stevens and Conway*, 1999]. The inversion algorithm is similarly the same as used for the MAHRSI observations [*Conway et al.*, 1999, 2000], although the degree of smoothing is adjusted based on slightly different uncertainties between the two instruments. Any systematic differences between the SHIMMER and MAHRSI OH results are therefore not due to either of these elements of the data processing.

[85] The radiance profile corresponding to the spectrum in Figure 13 is shown in Figure 14 along with the inverted OH number densities and corresponding uncertainties. As in the work of *Englert et al.* [2008], the uncertainties for this radiance profile are a root sum square (rss) combination of the statistical error (<7.5% between 70 and 80 km), an altitude-dependent systematic error due to the correction of grating imperfections (<10% between 70 and 80 km), and an altitude-independent 7% rss uncertainty in the OH g factors [*Englert et al.*, 2008; *Conway et al.*, 1999]. The statistical

uncertainty is derived from the residual of the averaged, calibrated spectrum after removing the modeled spectrum and thus implicitly accounts for the effects of the laboratory and on-orbit calibration corrections. The uncertainty of the absolute radiance calibration of the laboratory calibration source (±0.4%; see section 5.3) and the uncertainty introduced from the on-orbit instrument degradation, (<1%; see section 7.1) are not included in the uncertainties displayed in Figure 14 but are comparatively small. This results in a total radiance rss uncertainty of less than 14.5% between 70 and 80 km, which includes not only the statistical uncertainty but also the systematic uncertainties of the grating imperfections and the g factors. The uncertainties for each altitude are shown in Figure 14 for this example profile. Note that above ~77 km in Figure 14 the OH radiances are nearly proportional to the OH densities, since the nonlinear processes in the density retrieval, such as self-absorption, quenching, and near/far-field contributions are small. The effective lower boundary of our retrieval is 60 km. Despite the similarities in the spectral approach, this is not as low in altitude as MAHRSI was able to measure [*Conway et al.*, 2000]. We attribute this difference to the damage incurred by the interferometer during environmental testing (see section 4.1.4), which limited our ability to isolate the OH spectrum in the presence of the increasingly bright background as one moves below 60 km tangent altitude.

8.2. Comparison of SHIMMER OH With MLS OH and Photochemical Model Results

[86] Here we compare retrieved OH density profiles with concurrent observations and with one-dimensional photochemical models results. The concurrent data are from the 2.5 THz channel of MLS [*Pickett*, 2006; *Pickett et al.*, 2006, 2008], which has previously been compared with 1 day of SHIMMER data from July 2007 [*Englert et al.*, 2008]. The SHIMMER OH database now allows for a much more extensive comparison of OH densities over multiple years and latitude regions.

[87] Since the Aura satellite is in a Sun-synchronous orbit and since the SHIMMER observations are made during daytime, we compare the two data sets at local solar times (LTs) between 1300 and 1500. We previously found a very good agreement between OH observations of SHIMMER and MLS between 60 and 90 km, around 55°N and 1300 h LT in mid-July 2007 [*Englert et al.*, 2008]. Figure 15a shows a comparison using the same data, except that we have revised the SHIMMER data based on the on-orbit degradation inferred from the Rayleigh background peak brightness as indicated in Figure 11c. Because the SHIMMER data were assembled from relatively early in the mission (129 days into the mission), the brightness correction is only ~10% compared to the results previously presented by *Englert et al.* [2008, their Figure 2], which increases the OH densities by about the same amount. Peak mesospheric SHIMMER OH densities are nonetheless still in good agreement with peak MLS OH densities within the uncertainties of the experiments and also still in agreement with standard photochemical model results. The photochemical model [*Summers et al.*, 1997] uses standard JPL-06 reaction rates [*Sander et al.*, 2006] as well as zonally averaged MLS water vapor, pressures, and temperatures from the same day and latitude region.
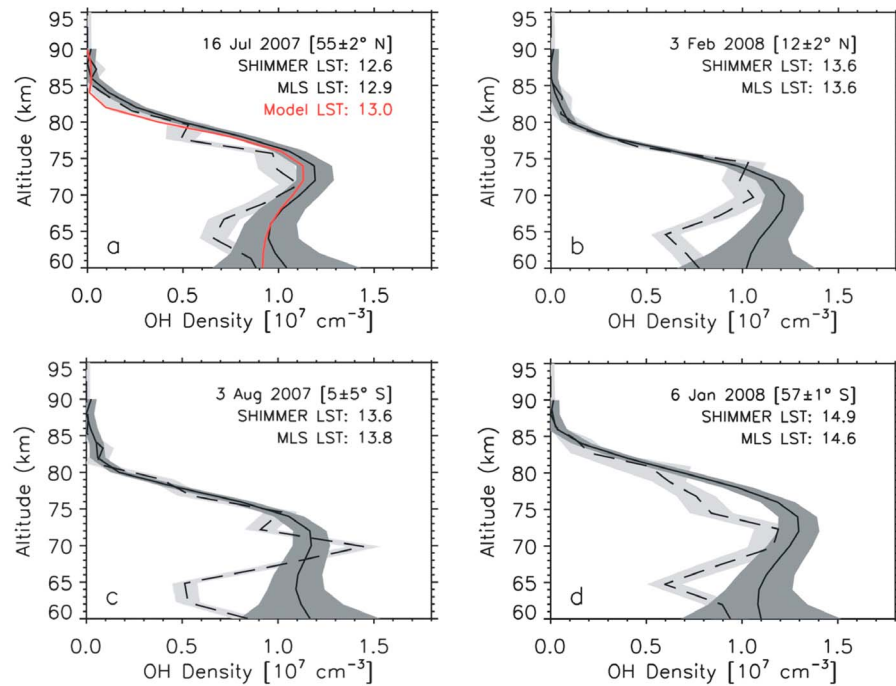
Figure 15. (a–d) SHIMMER OH density profiles in solid black from (a) 55°N, (b) 12°N, (c) 5°S, and (d) 57° S compared to concurrent MLS density profiles (dashed black line) for the same latitudes [*Pickett et al.*, 2008]. For each case, between 200 and 700 SHIMMER limb images were coaveraged during the day, and latitude region was indicated in each frame. A comparison with a standard photochemical model result is shown in Figure 15a (red). The model result convolved with the SHIMMER weighting functions to match the altitude resolution. The agreement of peak OH densities between SHIMMER and MLS is very good, with sporadic differences of up to ~20% in areas where MLS data show large altitude variations. The agreement between the SHIMMER profiles and the photochemical model result shown in Figure 15a is excellent, i.e., within about 5% near the peak.

[88] The good agreement of mesospheric OH observations by SHIMMER with standard photochemistry between 60 and 78 km in Figure 15a is in contrast to earlier MAHRSI results showing that mesospheric OH densities are 25%–35% lower than standard photochemical model results. However, this agreement is consistent within uncertainty with the independent analysis presented in Figure 12, showing that the MAHRSI measurements of Rayleigh scattered light are 24% lower than what SHIMMER measured under the same lighting conditions. In addition, independent mesospheric OH observations since the MARHSI missions by both MLS [*Pickett et al.*, 2008] and OSIRIS [*Gattinger et al.*, 2006] indicate mesospheric peak densities are not significantly smaller than standard photochemical model results and agree to within 20%. We also point out that the SHIMMER and MAHRSI observations were made at roughly the same phase of the solar cycle, namely the solar minima preceding and following solar cycle 23. Mesospheric OH directly responds to the solar Lyman α flux; however, a typical Lyman α flux variation of 10% or less during solar minimum corresponds to a change in OH density of only about 5% or less near the mesospheric OH peak. Thus, this variation is small compared to the discrepancy between the MAHRSI OH data and model results.

[89] To assess the repeatability of the MLS and SHIMMER agreement, we now explore comparisons over a wider variety of latitudes and different times of the year. In Figures 15b–

15d, we compare the two data sets at three different latitude regions from north to south: 12°N, 5°S, and 57°S. In each case, we have selected SHIMMER data that were taken at the same LTs as the MLS data. The cases shown in the four frames of Figure 15 span a period of nearly 7 months. In general, Figures 15b–15d show that peak SHIMMER OH densities are in good agreement with peak MLS OH densities and that the scale height above the peak is in excellent agreement, supporting the July 2007 comparison in Figure 15a. The largest discrepancy between the two data sets is in a relatively narrow altitude range near 65 km, where the MLS OH densities seem to show a bite out that is not present in the SHIMMER data. We also note that OSIRIS data do not show this bite out [*Gattinger et al.*, 2006].

[90] Figure 16 establishes the robustness of the 16 July 2007 model data comparison by presenting an analogous comparison performed on data from 19 August 2009, over 2 years later. As in Figures 15a and 16a, OH model results in Figure 16b use MLS water vapor, temperatures, and pressures from the same day. The overall agreement between observations and model results between 60 and 78 km is remarkably similar for both and provides additional validation of the SHIMMER OH data set. Above 78 km, the observed OH progressively becomes greater than the model. Since, as we have already noted, the retrieval of OH at these altitudes is relatively straightforward and the comparisons with MLS OH at these altitudes are very good (see Figure 15), this is a robust
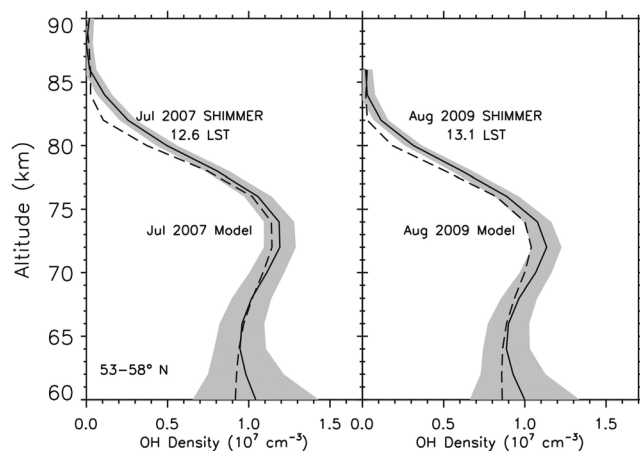
Figure 16. (left) OH density profile on 16 July 2007 compared with standard photochemical model results, reproduced from Figure 15a. The model results are multiplied with the SHIMMER weighting functions to match the altitude resolution. (right) Measured and modeled OH density profiles on 19 August 2009 (over 2 years later) for the same latitudes and at nearly the same time of year. The overall agreement between observations and model results is excellent in both cases.

result. One possibility for the model data difference above 78 km is the vertical redistribution of water vapor from polar mesospheric clouds [*Summers et al.*, 2001]. Although the model uses MLS water vapor, the vertical resolution of MLS water vapor near 80 km is 11–16 km [*Lambert et al.*, 2007] and considerably larger than the 3–7 km vertical resolution of the SHIMMER OH observations [*Englert et al.*, 2008]. Small-scale vertical structure in water vapor is therefore not necessarily captured by the model. Alternatively, since the photochemical lifetime of HO_x lengthens above 78 km, uncertainties in transport effects such as eddy diffusion may also need to be considered. These model data differences are local time dependent [*Englert et al.*, 2008] and are the subject of future study.

[91] The general consistency in the model data comparison shown in Figure 16 is particularly important, because it serves as an independent validation of the SHIMMER on-orbit degradation correction using the observed Rayleigh scattered background, discussed in section 7.1 (see also Figure 11c). For the calibrated brightnesses measured toward the end of the mission, like the ones used to retrieve the OH densities in Figure 16b, the brightness correction is about a factor of 2 compared with the early mission observations. We also note here that a 3 km altitude offset between the SHIMMER and MAHRSI Rayleigh background observations suggested by Figure 12e is not apparent in either the comparisons of SHIMMER OH observations against the MLS OH in Figure 15 or the model results in Figures 16. This provides additional evidence that there is a low pointing bias of 3 km in the MAHRSI OH data presented by *Conway et al.* [2000].

9. Conclusions

[92] We have provided comprehensive documentation of all aspects of the SHIMMER mission, including instrument design

and data analysis, as well as evidence that the SHIMMER OH data are of high quality throughout the 2.5 year long extended mission. This first flight of a Spatial Heterodyne Spectroscopy experiment on a free flying satellite was thus highly successful and accomplished its goal of validating the SHS technique for use in satellite remote sensing.

[93] Comparisons between SHIMMER and MLS OH data show good agreement at all reported altitudes (60–90 km) for several latitudes and seasons. While all MLS comparisons were necessarily made close to local noon, the low inclination of the STPSat-1 orbit and the resulting local time precession of the SHIMMER measurements yield unprecedented local time coverage of mesospheric OH, thus making the data set complementary to MLS.

[94] We found that the mesospheric OH densities measured by SHIMMER are in good agreement with standard photochemical model results between about 60 and 80 km and they do not show a 25%–35% mesospheric OH deficit previously reported using MAHRSI data. Analyzing the Rayleigh scattered background signals measured by MAHRSI and SHIMMER for similar conditions, albeit about 10 years apart, we found that MAHRSI signals are about 24% lower compared with SHIMMER observations, which we cannot explain with any change in the atmosphere or solar illumination. Using the same analysis, we also find a 3 km altitude low bias of the MAHRSI data used in the report by *Conway et al.* [2000] when compared with the SHIMMER data, possibly resulting from unique pointing operations during the second MAHRSI mission. We find no obvious indication of an altitude offset in our comparisons of SHIMMER OH results against MLS OH or the photochemical model results. Given that in addition to SHIMMER, neither MLS nor OSIRIS measurements were able to corroborate a mesospheric OH deficit in excess of 20%, we must consider that our findings suggest a previously unidentified MAHRSI calibration problem leading to the reported underestimate of mesospheric OH. Should that be the case, some conclusions that are based on MAHRSI observations need to be reexamined, whereas others likely remain unchanged. In particular, the mesospheric OH deficit [*Summers et al.*, 1997; *Conway et al.*, 1999] and the HO_x dilemma (which considered both upper stratospheric and mesospheric data) [*Conway et al.*, 2000], all of which rely on the absolute OH densities inferred by MAHRSI, should be revisited. On the other hand, the discovery of the Arctic summer mesosphere water vapor layer at the base of the PMC altitudes [*Summers et al.*, 2001], the first observations of ice particles formed by space shuttle exhaust [*Stevens et al.*, 2002], space shuttle exhaust contributing to polar mesospheric clouds, and the unexpected transport speed of space shuttle plumes [*Stevens et al.*, 2003] fundamentally do not rely on the absolute calibration of MAHRSI. Thus, these conclusions from the MAHRSI data should in principle remain unaffected.

References

Allen, M., J. I. Lunine, and Y. L. Yung (1984), The vertical distribution of ozone in the mesosphere and lower thermosphere, *J. Geophys. Res.*, *89*(D3), 4841–4872, doi:10.1029/JD089iD03p04841.

Anderson, J. G. (1971), Rocket measurement of OH in the mesosphere, *J. Geophys. Res.*, *76*(31), 7820–7824, doi:10.1029/JA076i031p07820.

Bernhardt, P. A., and C. L. Siefring (2006), New satellite-based systems for ionospheric tomography and scintillation region imaging, *Radio Sci.*, *41*, RS5S23, doi:10.1029/2005RS003360.

Bernhardt, P. A., C. L. Siefring, I. J. Galysh, and D. E. Koch (2010), A new technique for absolute total electron content determination using the CITRIS instrument on STPSat1 and the CERTO beacons on COSMIC, *Radio Sci.*, *45*, RS3006, doi:10.1029/2009RS004243.

Brault, J. W. (1987), High precision Fourier transform spectroscopy: The critical role of phase correction, *Mikrochim. Acta*, *3*, 215–227.

Canty, T., et al. (2006), Stratospheric and mesospheric HO_x: Results from Aura MLS and FIRS-2, *Geophys. Res. Lett.*, *33*, L12802, doi:10.1029/2006GL025964.

Cardon, J. G., C. R. Englert, J. M. Harlander, F. L. Roesler, and M. H. Stevens (2003), SHIMMER on STS-112: Development and Proof-of-Concept Flight, paper presented at AIAA Space 2003–Conference and Exposition, Long Beach, Calif., 23–25 Sept.

Conway, R. R., et al. (1996), Satellite measurements of hydroxyl in the mesosphere, *Geophys. Res. Lett.*, *23*(16), 2023–2096, doi:10.1029/96GL01401.

Conway, R. R., M. H. Stevens, C. M. Brown, J. G. Cardon, S. E. Zasadil, and G. H. Mount (1999), Middle atmosphere high resolution spectrograph investigation, *J. Geophys. Res.*, *104*(D13), 16,327–16,348, doi:10.1029/1998JD100036.

Conway, R. R., M. E. Summers, M. H. Stevens, J. G. Cardon, P. Preusse, and D. Offermann (2000), Satellite observations of upper stratospheric and mesospheric OH: The HO_x dilemma, *Geophys. Res. Lett.*, *27*(17), 2613–2616, doi:10.1029/2000GL011698.

Eckermann, S. D., et al. (2009), High-altitude data assimilation system experiments for the northern summer mesosphere season of 2007, *J. Atmos. Sol. Terr. Phys.*, *71*, 531–551.

Englert, C. R., B. A. Schimpf, M. Birk, and F. Schreier (2000), THOMAS 2.5 THz Measurements of Middle Atmospheric OH: Comparison With MAHRSI Observations and Model Results, in *Atmospheric Science Across the Stratopause, AGU Monogr.*, 123, edited by D. E. Siskind, S. D. Eckermann, and M. E. Summers, American Geophysical Union, Washington, D.C., pp. 305–310.

Englert, C. R., J. M. Harlander, J. G. Cardon, and F. L. Roesler (2004), Correction of phase distortion in spatial heterodyne spectroscopy, *Appl. Opt.*, *43*, 6680–6687.

Englert, C. R., and J. M. Harlander (2006), Flat-fielding in spatial heterodyne spectroscopy, *Appl. Opt.*, *45*, 4583–4590.

Englert, C. R., M. H. Stevens, D. E. Siskind, J. M. Harlander, F. L. Roesler, H. M. Pickett, C. von Savigny, and A. J. Kochenash (2008), First results from the Spatial Heterodyne Imager for Mesospheric Radicals (SHIMMER): Diurnal variation of mesospheric hydroxyl, *Geophys. Res. Lett.*, *35*, L19813, doi:10.1029/2008GL035420.

Gattinger, R. L., D. A. Degenstein, and E. J. Llewellyn (2006), Optical Spectrograph and Infra-Red Imaging System (OSIRIS) observations of mesospheric OH $A^2\Sigma^+$-$X^2\Pi$ 0-0 and 1-1 band resonance emissions, *J. Geophys. Res.*, *111*, D13303, doi:10.1029/2005JD006369.

Harlander, J. M., R. J. Reynolds, and F. L. Roesler (1992), Spatial heterodyne spectroscopy for the exploration of diffuse interstellar emission lines at far ultraviolet wavelengths, *Astrophys. J.*, *396*, 730–740.

Harlander, J. M., F. L. Roesler, C. R. Englert, J. G. Cardon, R. R. Conway, C. M. Brown, and J. Wimperis (2003), Robust monolithic ultraviolet interferometer for the SHIMMER instrument on STPSat-1, *Appl. Opt.*, *42*, 2829–2834.

Kudo, K., T. Arei, and T. Ogawa (1970), Method for determining the degrees of polarization of infrared polarizers and monochromators, *J. Opt. Soc. Am.*, *60*, 1046–1050.

Kurucz, R., I. Furenlid, J. Brault, and L. Testerman (1984), *National Solar Observatory Atlas*, vol. 1, Harvard Univ. Press, Cambridge, Mass.

Lambert, A., et al. (2007), Validation of the Aura Microwave Limb Sounder middle atmosphere water vapor and nitrous oxide measurements, *J. Geophys. Res.*, *112*, D24S36, doi:10.1029/2007JD008724.

Lean, J. L., et al. (1997), Detection and parameterization of variations in solar mid- and near-ultraviolet radiation (200–400 nm), *J. Geophys. Res.*, *102*(D25), 29,939–29,956, doi:10.1029/97JD02092.

Meier, R. R., et al. (2010), Can molecular diffusion explain space shuttle plume spreading?, *Geophys. Res. Lett.*, *37*, L08101, doi:10.1029/2010GL042868.

Morgan, M. F., D. G. Torr, and M. R. Torr (1993), Preliminary measurements of mesospheric OH $X^2\Pi$ by ISO on ATLAS 1, *Geophys. Res. Lett.*, *20*(6), 511–514, doi:10.1029/92GL02628.

Pickett, H. M. (2006), Microwave Limb Sounder THz Module on Aura, *IEEE Trans. Geosci. Remote Sens.*, *44*, 1122, doi:10.1109/TGRS.2005.862667.

Pickett, H. M., B. J. Drouin, T. Canty, L. J. Kovalenko, R. J. Salawitch, N. J. Livesey, W. G. Read, and J. W. Waters (2006), Validation of Aura MLS HO_x measurements with remote-sensing balloon instruments, *Geophys. Res. Lett.*, *33*, L01808, doi:10.1029/2005GL024048.

Pickett, H. M., et al. (2008), Validation of Aura Microwave Limb Sounder OH and HO_2 measurements, *J. Geophys. Res.*, *113*, D16S30, doi:10.1029/2007JD008775.

Rodrigo, R., J. J. Lopez-Moreno, M. Lopez-Puertas, F. Moreno, and A. Molina (1986), Neutral atmospheric composition between 69 and 220 km: A theoretical model for midlatitudes, *Planet. Space Sci.*, *34*, 723–743.

Russell, J. M., III, et al. (2009), The Aeronomy of Ice in the Mesosphere (AIM) mission: Overview and early science results, *J. Atmos. Sol. Terr. Phys.*, *71*, 289–299.

Sander, S. P., et al. (2006), Chemical kinetics and photochemical data for use in atmospheric studies, *JPL Publ., 06-2*.

Siefring, C. L., P. A. Bernhardt, P. A. Roddy, and D. E. Hunton (2009), Comparisons of equatorial irregularities measurements from C/NOFS: TEC using CERTO and CITRIS with in situ plasma density, *Geophys. Res. Lett.*, *36*, L00C08, doi:10.1029/2009GL038985.

Siskind, D. E., M. H. Stevens, J. T. Emmert, D. P. Drob, A. J. Kochenash, J. M. Russell III, L. L. Gordley, and M. G. Mlynczak (2003), Signatures of shuttle and rocket exhaust plumes in TIMED/SABER radiance data, *Geophys. Res. Lett.*, *30*(15), 1819, doi:10.1029/2003GL017627.

Stevens, M. H., and R. R. Conway (1999), Calculated OH $A^2\Sigma^+$-$X^2\Pi$(0,0) band rotational emission rate factors for solar resonance fluorescence, *J. Geophys. Res.*, *104*, 16,369–16,378, doi:10.1029/1998JD100073.

Stevens, M. H., C. R. Englert, and J. Gumbel (2002), OH observations of space shuttle exhaust, *Geophys. Res. Lett.*, *29*(10), 1378, doi:10.1029/2002GL015079.

Stevens, M. H., et al. (2003), Polar mesospheric clouds formed from space shuttle exhaust, *Geophys. Res. Lett.*, *30*(10), 1546, doi:10.1029/2003GL017249.

Stevens, M. H., R. R. Meier, X. Chu, M. T. DeLand, and J. M. C. Plane (2005), Antarctic mesospheric clouds formed from space shuttle exhaust, *Geophys. Res. Lett.*, *32*, L13810, doi:10.1029/2005GL023054.

Stevens, M. H., et al. (2008), First UV satellite observations of mesospheric water vapor, *J. Geophys. Res.*, *113*, D12304, doi:10.1029/2007JD009513.

Stevens, M. H., et al. (2009), The diurnal variation of polar mesospheric cloud frequency near 55°N observed by SHIMMER, *J. Atmos Sol. Terr. Phys.*, *71*, 401–407.

Stevens, M. H., et al. (2010), Tidally induced variations of PMC altitudes and ice water content using a data assimilation system, *J. Geophys. Res.*, *115*, D18209, doi:10.1029/2009JD013225.

Summers, M. E., et al. (1997), Implications of satellite OH observations for middle atmospheric H_2O and ozone, *Science*, *277*, 1967–1970, doi:10.1126/science.277.5334.1967.

Summers, M. E., et al. (2001), Discovery of a water vapor layer in the Arctic summer mesosphere: Implications for polar mesospheric clouds, *Geophys. Res. Lett.*, *28*(18), 3601–3604, doi:10.1029/2001GL013217.

C. R. Englert, M. H. Stevens, and D. E. Siskind, Naval Research Laboratory, Space Science Division, 4555 Overlook Ave. SW, Code 7640, Washington, DC 20375-5320, USA. (christoph.englert@nrl.navy.mil)

J. M. Harlander, Department of Physics, Astronomy and Engineering Science, Saint Cloud State University, 720 4th Avenue South, St. Cloud, MN 56301-4498, USA.

F. L. Roesler, Department of Physics, University of Wisconsin-Madison, 1150 University Avenue, Madison, WI 53706-1390, USA.